

1 Colour remote sensing of the impact of artificial light at
 2 night (II): Calibration of DSLR-based images from the
 3 International Space Station

4 Alejandro Sánchez de Miguel^{a,b,c,d,*}, Jaime Zamorano^b, Martin Aubé^c,
 5 Jonathan Bennie^e, Jesús Gallego^b, Francisco Ocaña^{b,f}, Donald R. Pettit^g,
 6 William L. Stefanov^h, Kevin J. Gaston^a

7 ^a*Environment and Sustainability Institute, University of Exeter, Penryn, Cornwall TR10*
 8 *9FE, U.K.*

9 ^b*Depto. Física de la Tierra y Astrofísica. Instituto de Física de Partículas y del Cosmos*
 10 *(IPARCOS), Universidad Complutense, Madrid, Spain*

11 ^c*Physics dept., CEGEP de Sherbrooke, Sherbrooke, J1E 4K1, Canada*

12 ^d*Instituto de Astrofísica de Andalucía, Glorieta de la Astronomía, s/n, C.P.18008 Granada,*
 13 *Spain*

14 ^e*Centre for Geography and Environmental Science, University of Exeter, Penryn, Cornwall*
 15 *TR10 9FE, UK*

16 ^f*Quasar SR for ESA, European Space Astronomy Centre, E-28691 Villanueva de la*
 17 *Cañada, Spain*

18 ^g*Astronaut Office, Flight Operations Directorate, NASA Lyndon B. Johnson Space Center,*
 19 *Houston, Texas, USA*

20 ^h*Exploration Science Office, Astromaterials Research and Exploration Science Division,*
 21 *Exploration Integration and Science Directorate, NASA Lyndon B. Johnson Space Center,*
 22 *Houston, Texas, USA*

23 **Abstract**

Nighttime images taken with DSLR cameras from the International Space Station (ISS) can provide valuable information on the spatial and temporal variation of artificial nighttime lighting on Earth. In particular, this is the only source of historical and current visible multispectral data across the world (DMSP/OLS and SNPP/VIIRS-DNB data are panchromatic and multispectral in the infrared but not at visible wavelengths). The ISS images require substantial processing and proper calibration to exploit intensities and ratios from the RGB channels. Here we describe the different calibration steps, addressing in turn Decodification, Linearity correction (ISO dependent), Flat field/Vignetting, Spectral characterization of the channels, Astrometric calibration/georeferencing, Photometric calibration (stars)/Radiometric correction (settings correction - by exposure time, ISO, lens transmittance, etc) and Transmittance correction (win-

*Corresponding author
 Preprint submitted to *Earth and Space Science* (Alejandro Sánchez de Miguel)

dow transmittance, atmospheric correction). We provide an example of the application of this processing method to an image of Spain.

24 *Keywords:* artificial lighting, light pollution, night, remote sensing, urban

25 **1. Introduction**

26 There is growing demand for colour imagery of the Earth at night. This
27 has particularly been driven by increasing recognition of the impacts of outdoor
28 artificial nighttime lighting (from streetlights and other sources) on the nat-
29 ural environment, human health, and associated policy and public concerns
30 (e.g. Rich and Longcore (2013); Hölker et al. (2010); Falchi et al. (2011);
31 Gaston et al. (2012, 2015); Gaston (2013, 2018); Garcia-Saenz et al. (2018)).
32 These impacts are not only influenced by the spatial extent, the timing and
33 the intensity of that lighting, but also by its spectrum. This last consider-
34 ation limits the insights that can be obtained from the vast majority of his-
35 torical and current sources of geographic scale data on the occurrence of such
36 lighting, including data from the Defense Meteorological Program/Operational
37 Line-Scan System (DMSP/OLS; Elvidge et al. (1997)) and from the Suomi-
38 National Polar-Orbiting Partnership/Visible and Infrared Imaging Radiometer
39 Suite - Day/Night Band (SNPP/VIIRS-DNB; Elvidge et al. (2013)).

40 By far the most important source of colour imagery of the Earth at night
41 is that obtained from the International Space Station (ISS) by the astronauts
42 and cosmonauts of the five space agencies that constitute the ISS consortium:
43 NASA, ESA, JAXA, CSA-ASC and ROSCOSMOS (Stefanov et al. (2017, 2019a)).
44 Between 2002 and 2018, more than 3 million images have been taken by the crew
45 of the ISS, of which 1.34 million were taken at night (sun elevation less than 0
46 degrees). The diurnal and nocturnal images from NASA, CSA-ASC and ESA
47 are stored in the NASA archive (<http://eol.jsc.nasa.gov>; Stefanov et al. (2017,
48 2019a)). Some, but not all, of the images taken by JAXA and ROSCOSMOS
49 are also stored in the NASA archive. The scientific value of these images is
50 immense, as they constitute the only large public dataset with nighttime colour

51 information obtained from space over the last 17 years (Levin et al., 2020). Due
52 to the limitations of data from the VIIRS and DMSP satellites, this dataset
53 is key to determining change in visible artificial lighting over this long period
54 (Kyba et al. (2017); Sánchez de Miguel et al. (2019)).

55 The camera bodies and lenses used by the astronauts to take images of the
56 Earth have mainly been from Nikon’s professional product line (see Table 1 for
57 those used for nocturnal photography). These have usually been unmodified,
58 with the exception of the Nikon D3S S/N:2007944 used on missions ISS030 and
59 ISS031 that had the infra-red filter removed. Most of the Nikon cameras used
60 have had a CMOS sensor, although the Kodak 760C and the Nikon D1 that
61 were used had CCD sensors (Waltham (2013)). All the cameras have a Bayer
62 filter that provides simultaneous images in three colours (two green, one red and
63 one blue).

64 The environmental conditions on the ISS are strictly controlled, with tem-
65 perature at $24^{\circ}\text{C} \pm 2^{\circ}\text{C}$, pressure around 745-721 mmHg, and relative humidity
66 around 60%. This means that the cameras have not only been operating well
67 within their nominal environmental ranges but effectively in constant environ-
68 mental conditions. Although cameras have been used during extravehicular
69 activity (EVA) or in external experiments, principally windows in the cupola
70 and elsewhere on the ISS enable astronauts to take images of the Earth from a
71 wide variety of angles. The ground track of the ISS covers nadir latitudes from
72 51.6°N to 51.6°S , at an altitude of approximately 405 km, although this can
73 vary in the range of 330 to 435 km. Usually images have been taken by astro-
74 nauts using cameras that are handheld. Pettit (2009) developed a prototype
75 system that partially compensated for movement during image acquisition and
76 was used during mission ISS006. Later missions, like ISS030 to ISS040, have
77 employed a special tripod (Nightpod; Sabbatini (2014)). At least for images
78 held in the open NASA archive there is no information on their acquisition be-
79 yond the metadata of the images themselves, thus it is not easy and frequently
80 impossible to attribute them to a specific window, tracking device or operator.
81 Only when an astronaut posts their own images, on Twitter for example, can

82 we have reasonable confidence in their authorship.

83 A growing number of science studies have attempted to use images taken
84 from the ISS in their raw or crudely enhanced forms (Venzke et al., 2009; Lock-
85 wood and Hazlett, 2013; Anderson et al., 2010; Levin and Duke, 2012; Liu et al.,
86 2011; Metcalf, 2012; Kuechly et al., 2012; Mazor et al., 2013; Sánchez de Miguel
87 et al., 2014; Li et al., 2014; So, 2014; Kyba et al., 2014; Rybnikova and Port-
88 nov, 2017, 2018; Xu et al., 2018; Levin et al., 2020). Indeed, the only research
89 work we are aware of that made some attempt to address issues of calibration
90 is that of So (2014), which used a dark subtraction, and those in which the cur-
91 rent team has been involved (Zamorano et al., 2011; Sánchez de Miguel, 2015;
92 Garcia-Saenz et al., 2018, 2019; Hale and Arlettaz, 2019; Bará, 2020; Pauwels
93 et al., 2019; Sánchez de Miguel et al., 2019, 2020). The effects of this lack of
94 calibration can be very different from study to study and need to be considered
95 carefully. Unfortunately, in many cases calibration of images taken by astro-
96 nauts from the ISS will be necessary in order to provide accurate representations
97 of the colour composition of scenes, and this is not a trivial task.

98 In a previous paper (Sánchez de Miguel et al., 2019), we described the use
99 of colour-colour diagrams to analyse images taken by astronauts on the ISS and
100 to estimate spatial and temporal variation in the spectrum of artificial lighting
101 emissions. In this paper we provide a methodology for calibrating such images.
102 The approach that we describe is also relevant to the calibration of images taken
103 with standard DSLR cameras for other purposes, including meteor science (me-
104 teor photometry - Borovička et al. (2014); meteor video photometry - Madiedo
105 et al. (2019); meteor spectroscopy - Cheng and Cheng (2011)), measurement of
106 skyglow (Hänel et al., 2018), and more generally scientific photography using
107 DSLR cameras with antiblooming. In order to use well characterized standard
108 emitters, we use stars as calibration sources, as the variability and stability of
109 their spectra is well known. Indeed, laboratory calibration sources typically
110 have a precision of 0.2% (Wolfe, 1998), whilst calibration by stars can attain
111 precisions of 0.001% (Poddaný et al., 2010). This technique also allows us to use
112 multiple calibrations from onboard the ISS that are stable in time and that ac-

113 count for the window through which images were obtained. A similar technique
114 has also been proposed for calibration of data from the SNPP/VIIRS-DNB
115 (Fulbright and Xiong, 2015) and was suggested first by Zamorano et al. (2011).

116 Calibration of images of the earth acquired from the ISS requires a num-
117 ber of steps that we will address in turn (Fig. 1): Decodification, Linearity
118 correction (ISO dependent), Flat field/Vignetting, Spectral characterization of
119 the channels*, Astrometric calibration*/georeferencing, Photometric calibration
120 (stars)*/ Radiometric correction (settings correction - by exposure time, ISO,
121 lens transmittance, etc) and Transmittance correction (window transmittance,
122 atmospheric correction). The steps marked with an asterisk may not be re-
123 quired for some specific science cases (e.g. differential evolution time - Meier
124 (2018); Bará et al. (2019); edge detection - Kotarba and Aleksandrowicz (2016)).
125 Neglecting any particular correction should always explicitly be justified.

126 In this paper, we will focus primarily on calibration of images taken with the
127 Nikon D3S (for calibration equipment see Supplementary Information) because
128 this is the best studied case and the camera that has been used most intensively
129 for nocturnal photography at the ISS over the two last decades (from mission
130 ISS026 until mission ISS045). However, in general, with small adjustments, the
131 procedures described can be applied to any other digital camera, and we will
132 consider all of the cameras used at the ISS (Table 1) and highlight the differences
133 between them when it is relevant. The Nikon D3S has a 12.1 megapixel sensor
134 equivalent to a full frame (35mm) and was announced by Nikon Corporation
135 on 14 October 2009. It has interchangeable lenses using the F-mount, an ISO
136 range from 200 to 12800, and 14-bit A/D conversion.

137 **2. Calibration steps**

138 *2.1. Step 1: Decodification*

139 A DSLR camera obtains information as photons of light that produce elec-
140 trons, and these electrons are effectively stored in pixels of the CCD/CMOS
141 chip. The electrons are trapped by the nearest potential well (one per pixel)

142 and digitalized by an analogue conversion (DA Converter) sensor that measures
143 the electrical potential on the wells of the chip. Whilst in some professional
144 cameras a non-destructive read out is possible (Nakamura et al., 1995), most
145 CCD/CMOS chips are read by measuring the current when it passes through
146 the DA converter (Fowler and El Gamal, 1995; Fossum et al., 2000). This in-
147 formation is pre-processed and saved as a data file. This file is usually coded
148 in a proprietary format, and in the case of Nikon cameras, this is called NEF.
149 This is what is called a RAW file. The first step in the calibration process is
150 the decodification of this file, taking the data coded in the proprietary format
151 and transforming it into a readable open format, such as TIFF (Desk, 1992) or
152 FITS (Hanisch et al., 2001), without losing crucial information or changing the
153 physical meaning.

154 Even so-called RAW files from a DSLR tend to have undergone some pre-
155 processing. A pure ideal CCD/CMOS RAW file coming from an ideal sensor
156 will have three components: (i) the signal itself, (ii) an artificial signal (bias)
157 included on the sensor to avoid negative values in the process of digitalization,
158 and (iii) Gaussian noise plus an additive constant (dark current) arising from
159 the sensor's sensitivity to heat. On our reference camera, the Nikon D3s, and
160 all subsequent versions except the Nikon D5, a complex hardware treatment is
161 applied to the signal (Koyama and Jiang, 2011; Sánchez de Miguel, 2015). This
162 treatment means that we do not need to do any bias or dark correction in these
163 cases, but noise effects need to be controlled. DSLR sensors are capable of a
164 16-bit dynamic range. However, in practice on commercial models it is 14 or
165 12 bits, because saving 16-bit information takes too much time. This means
166 that some detailed information is lost in the digitalization process with a loss
167 of dynamic range.

168 The current most widely used software to undertake decodification is DCRAW
169 (Coffin, 2008) and the most conservative decodification options are: -6 that
170 means 16 bit extraction, -o 0 that means no color balance, -H 1 that means
171 nothing excluded, and -v to show any error in the decodification process.

172 *2.2. Step 2: Linearity correction*

173 While most scientific camera sensors force linearity between numbers of in-
174 cident photons and pixel signal strength as a key characteristic, commercial
175 DSLR cameras have sensors with an anti-blooming function. By using an over-
176 flow channel, this system ensures that when a well of the chip is saturated then
177 excess electrons do not contaminate adjacent wells (as can happen with regular
178 CCD or CMOS sensors)(Sakai et al., 2009). This produces a roughly linear
179 response in the pixel signal when high gain is used. Unfortunately, there are no
180 details available of the specific technology used for the Nikon DX sensors. Cur-
181 rently, we have not detected differential absorption by chip substrate, although
182 this could be investigated further in future versions of the processing pipeline.

183 Typically, the gain of the camera operates to an ISO standard (ISO 12232:2006
184 (E), 2006). Fig. 2 shows the effect of anti-blooming when a camera is exposed
185 to a stable light source across all of the different exposure times that the camera
186 is able to produce. This effect can be compensated by characterization of this
187 response for a particular ISO. Even if a camera is in principle calibrated to the
188 ISO standard, this still allows a 20% error, and there can be differences on the
189 different channels. Indeed, without corrections, bad colour information (aka.
190 band ratios, see Sánchez de Miguel et al. (2019)) can be produced. As Metcalf
191 (2012) found, radiance values can be underestimated, and radiance ratios can
192 appear variable even if they are stable.

193 Having characterised the response of the camera for a particular ISO, the
194 intensity values of an image that has been taken using this can be divided by
195 these corrected ones. Those over the range of the linear response will not change
196 (aka. under ~ 17.000 ADU) whilst those in the range of the non-linear response
197 will be linearized.

198 *2.3. 2.3 Step 3: Flat field*

199 A wide range of lenses have been used with DSLRs on the ISS, from fish
200 eyes to telephotos. A few have been used for long periods, but others on just
201 a single mission. These lenses introduce various additional calibration issues.

202 The first of these is flat field/illumination/vignetting correction. This is a very
203 standard correction with DSLR imagery, although unfortunately not usually
204 addressed with imagery from the ISS (see (Burggraaff et al., 2019) for standard
205 corrections to consumer cameras). This correction consists of the acquisition of
206 shots from a uniform emitting source (aka. flat field), so that any heterogeneity
207 in the acquired image is the result of vignetting of the lens and linearity effects.
208 Distortion effects, such Barrel, Pincushion, and Mustache can also be corrected.
209 However, this should be avoided unless absolutely necessary because of the
210 challenges of combining such corrections with those necessary due to the angular
211 perspective at which many ISS images are obtained as a consequence of the
212 Earth’s curvature, and because performing several successive distortions will
213 amplify errors (Cardiel et al., 2002)) (see 2.7 Step 6).

214 Images of star fields from the ISS are not available for all combinations of
215 cameras and lenses that have been used to obtain images of the Earth. In order
216 to translate the light intensity measured using one lens to that which would
217 be measured using another the light transmission of the optical elements of the
218 latter needs to be considered. The f/ number can give a first order idea of
219 this in a standardised way. However, this is not sufficiently accurate for many
220 purposes, so instead the Transmission coefficient (T number) of the lens needs
221 to be measured. Table 2 provides these values, as well as the f/ number for
222 some of the most frequently used lenses on the ISS. Values in this table have
223 been calculated using the SaveStar Consulting S.L. lab by acquiring images of
224 a 4 ± 0.1 lux illuminated lambertian surface. The light Source was a tungsten
225 filament.

226 Note that in general the apertures of lenses can be closed down to provide
227 sharper images. When this happens, the diaphragm rarely closes to exactly
228 the same position (except when fully open), so it is recommended that imagery
229 is taken using maximum apertures (explained in more detail in 2.5 Step 5c).
230 On bright sources this can be considered a compromise between sharpness of
231 images, signal to noise ratios, and photometric accuracy. Fortunately, this has
232 been done for most of the images taken at night from the ISS.

233 *2.4. Step 4: Astrometric calibration*

234 The astronauts do not only acquire images of cities at night. They also
235 acquire lots of other kinds of nocturnal images, including of auroras, sunsets,
236 and occasionally also star fields. The "Cities at Night" project has a NASA
237 archive selection of these images (Cities at night collaboration, 2015). They
238 can be used for several purposes, such as calculating lens distortion and lens
239 transmittance, or as we do in this case, for radiometric calibration.

240 Once the characteristics of a camera and lens have been determined it is
241 necessary to use standard sources to calibrate the imagery of the Earth that
242 has been taken. The use for this purpose of starfield images taken from the ISS
243 has the great advantage that they were obtained with the equipment under the
244 same temperature, pressure and humidity conditions as the images of the Earth.
245 They will also have been acquired through windows with the same reflection and
246 transmission characteristics; light transmission through the windows is very high
247 except for some Zvezda windows (we can assume that absorption in all bands
248 is less than 5% in the visible regime, although windows in the Destiny lab show
249 significant transmission reduction beyond the NIR), and special coatings have
250 been used to avoid reflections (see 2.9 Step 8).

251 The first step in using starfield images as standard sources is astrometric
252 calibration, determining the coordinates of the stars in each image. This can be
253 done using standard astronomical methods. We use the software Astrometry.net
254 (Lang et al., 2010). This automatically spatially calibrates an image, so that
255 each pixel has corresponding celestial coordinates. Moreover, it extracts the
256 sources and identifies them using a catalog. Stars are the flux standard sources
257 that we will subsequently use.

258 Astrometric calibration (also called the World Coordinate System) by As-
259 trometry.net provides direction, orientation and plate scale (transformation be-
260 tween the apparent angular separation and linear separation at the focal plane).
261 The software does not require any additional input, and makes a blind cal-
262 ibration using only the image. It is a powerful tool as there is no need to
263 know spacecraft attitude nor window orientation nor the direction in which an

264 astronaut was pointing the camera. It has also been used successfully in non-
 265 stabilised high-altitude balloon observations where attitude is not controlled
 266 (Ocaña, 2017; Ocaña et al., 2019).

267 *2.5. Step 5a: Photometric calibration on board*

268 To perform photometric calibration, we need a standard source. As there
 269 are no electronic standard flux sources onboard of the ISS the most accurate
 270 method of calibration is using the stars, as has been proposed for other satellites
 271 (Fulbright and Xiong, 2015) and as is routinely done in astronomy.

272 We will focus on use of a selection of stars from Ducati (2002). Even though
 273 stars are very well characterized light sources, there are differences between the
 274 filters that were used in making those measurements and those used in DSLR
 275 cameras. To solve this problem we can use a statistical correction based on the
 276 synthetic photometry technique (Straizys, 1996; Sánchez de Miguel et al., 2017,
 277 2019):

$$278 \quad GN = V + 0.1291(2) \times (B - V) - 0.0051(2) \quad (1)$$

$$279 \quad BN = GN + 0.6123(7) \times (B - V) - 0.0340(6) \quad (2)$$

$$RN = GN + 0.0262(3) + 0.5880(5) \times (R - V) \quad (3)$$

280 where BN, RN and GN are the respective RGB bands of the DSLR image, and
 281 B, V and R are Johnson bands (an astronomical standard); these relationships
 282 are shown in Fig. 3. These corrections have been calculated for the spectral
 283 response of the D3S although, as can be seen in Sánchez de Miguel et al.
 284 (2019), all Nikon cameras have extremely similar spectral responses. Once these
 285 corrections to the intensities of the stars are applied, the transformation from
 286 data numbers to radiometry units is immediate by applying a linear fit (see Fig.
 287 4).

288 As the Ducati (2002) catalogue has few stars in the dim part of the cali-
 289 bration and only 18 stars in total, for verification purposes we used the Tycho
 290 catalogue (Hog et al., 2000), which contains many more stars. Fig. 5 shows the

291 effect of the saturation of the brightest stars. Future analysis can be done the
292 new catalog Cardiel et al. (2021), specifically designed for DSLR cameras.

293 By using these methods we get the correspondence between the radiance and
294 the data numbers in magnitudes. To convert this on the international system
295 of units we need to use:

$$AB = -2.5 \log_{10}(flux) - 5 \log_{10}(w) + 2.401 \quad (4)$$

296 where AB is in $mag/arcsec^2$, flux in $nW/cm^2/sr/\text{\AA}$, and w is wavelength in \AA
297 (Sánchez de Miguel et al., 2017).

298 When we calibrate a starfield image taken from the ISS, we do not need
299 to apply any atmospheric correction, as is usually done when this technique is
300 used with starfield images taken from the ground, because the ISS is at 400 km
301 above the Earth and the density of the atmosphere there is negligible and for
302 this purpose is considered to be a vacuum (at this elevation pressure is even
303 higher than that of the regular vacuum labs on Earth, from 10^{-6} to 10^{-9} torr
304 (Finckenor and de Groh, 2017), compared to the 760 torr of the atmosphere at
305 sea level).

306 *2.5.1. Step 5b: Photometric calibration from the ground*

307 As previously mentioned, some images of the Earth taken from the ISS have
308 been obtained using lenses for which starfield images are not available (for exam-
309 ple, because their focal lengths make it impossible to take sharp starfield images
310 given the speed of movement of the ISS). For those cases when starfield cali-
311 bration is not possible, the solution is to apply a standard absolute photometry
312 technique to achieve photometric calibration of the lens from the ground.

313 For observations taken from the ground the light of the stars travels through
314 the atmosphere and suffers absorption, scattering, and dispersion depending on
315 the wavelength. The amount of extinction (the combined effect) depends on the
316 extinction coefficient of the atmosphere at this time and on the length of the
317 path of the light across the atmosphere. As a result, the flux density (in units
318 of $ergs/s/cm^2/\text{\AA}$) measured on the ground for a star is lower than the flux at

319 the top of the atmosphere:

$$F(\text{observed}) = F_o \cdot 10^{-0.4KX} \quad (5)$$

320 where F_o is the flux outside the atmosphere (which we know since we are ob-
321 serving standard stars), K is the extinction coefficient for this wavelength, and
322 X the airmass calculated as $X = \sec z$ (this formula is only usable for zenith
323 angles up to about 60° to 75° ; for more accurate version see 2.8 Step 7), z be-
324 ing the zenith angle ($90 - \text{elevation above horizon}$). We call photometric nights
325 those clear nights with constant transparency (see definition of photometric
326 night at <https://www.eso.org/sci/observing/phase2/ObsConditions.html>). For
327 these nights the extinction coefficient is constant for the whole night. Observing
328 several standard stars through the night at different heights above the horizon
329 we can derive this coefficient and the zero point of the photometry for each
330 photometric band. The derived zero point of the photometric band is valid for
331 this observational setup (camera, lens, ISO, and f number) regardless of the
332 night of the observation, i.e. it depends only on the instrumentation. So, the
333 atmospheric effects only need to be considered on the particular night that the
334 calibration images are acquired.

335 2.5.2. Step 5c: Setting adjustments

336 It is not possible to have images calibrated for all of the possible cameras
337 and settings. So, we scale the adjustments to 50 mm f/1.4. It is well known
338 that the repeatability of mechanical iris-type lens diaphragms is limited, having
339 a noticeable tolerance. The blades move back and forth during each image
340 acquisition, limiting the entrance pupil to approximately the same position but
341 not exactly so (Chylinski, 2012), creating so-called ‘aperture flickering’. We
342 have created a model to estimate the potential effect of closing the shutter but
343 the current one is a general correction with the f/ number:

$$L_0 = 2 \times f^{-2} \text{ or } Tn \quad (6)$$

$$\text{Correction factor} = 1/(ISO/100) \times C_0/T/B_N \times C_1/L_0 \quad (7)$$

344 where, ISO is the ISO 12232:2006 standard for digital photography, C_0 is a
345 correction for the sensitivity of the camera model, T is the exposure time, B_N
346 is the correction for the bit rate, and C_1 is the colour correction between different
347 camera models. L_0 is the correction for the aperture expressed as the f number
348 or the T_n true transmission of the lens when the shutter is fully open (see Table
349 2). Some of these settings can have up to 15% error according to the ISO
350 12232:2006 standard.

351 **3. Step 6: Georeferencing**

352 Images of the earth from the ISS need to be georeferenced to establish the
353 link between image pixels and actual points on the ground. The time of ac-
354 quisition of each image is known but, although the orbit of the ISS is precisely
355 defined, unfortunately this does not provide sufficient information. The time
356 stamp data are not precise enough to define a nadir location (errors may be
357 more than 1000 km), and an image may be taken in a direction that departs
358 substantially from the nadir. A major citizen science program, “Cities at Night”
359 (<http://www.citiesatnight.org>, (Sánchez de Miguel et al., 2014)), is being used to
360 automate the georeferencing of large numbers of ISS images by identifying the
361 urban areas that these represent. More generally, and where sufficient control
362 points cannot automatically be identified, georeferencing can be done manu-
363 ally, for which purpose we have used QGIS (Team et al., 2015) and Global
364 Mapper (Geographics, 2011). Several Python libraries have been used in this
365 process, like NumPy (Oliphant, 2006), AstroPy (Robitaille et al., 2013) and
366 GDAL (Warmerdam, 2008). The preferred sampling method is bilinear for the
367 pixels and thin plate spline for the coordinates. The number of recommended
368 control points can depend a lot on the inclination of the image and lens. For
369 nadir and 400 mm, 20 control points can be enough to reach RMSE 2.5 pix-
370 els using polynomial third degree fitting. For tilted images taken with a 24
371 mm, for example, more than 100 points would be needed and with 400 points
372 can be visually indistinguishable from a comparison layer (VIIRS); the only

373 transformations able to rectify deformations on tilted images are Thin Plane
 374 Splines that provide unrealistic values of RMSE - a conservative estimation can
 375 be RMSE ~ 4 pixels, but more research is needed to systematise this analysis.

376 3.1. Step 7: Atmospheric correction

377 Whilst no atmospheric correction is required for starfield images taken from
 378 the ISS, this needs to be done for images taken of the Earth. The procedure
 379 selected depends on the concept of airmass. In astronomy, one airmass is equiv-
 380 alent to the volume of atmosphere in the direction of the zenith of an observer
 381 on the ground (that is equivalent to the same volume of mass to an observer
 382 located in orbit looking to the nadir at the same geographical coordinates).
 383 Using this approach it is straightforward to estimate the equivalent volume of
 384 atmosphere at different zenith angles or the corresponding nadir angles. The
 385 formula $X = \sec z$, as above, can be used up to 80 degrees of zenith angle con-
 386 sidering a plane parallel approximation of atmosphere with about 3% error and
 387 for higher angles several models are available (e.g. Pickering (2002)). Then, we
 388 can atmospherically correct each image using:

$$I/I_0 = 10^{X_h(h) \times K / -2.5} \quad (8)$$

389 where X_h is the airmass function of the height, h is the height (in metres), I
 390 is the observed intensity, I_0 the intensity with atmospheric effect, and K is the
 391 extinction coefficient (derived from Harwit (1973)). The extinction coefficient
 392 for 1 air mass can be calculated as:

$$K = A_{ray} + A_{aer} + A_{oz} \quad (9)$$

393 where A_{ray} is Raleigh scattering, A_{aer} the absorption by aerosols, and A_{oz} the
 394 absorption by ozone. Using the definitions compiled in García Gil et al. (2012):

$$A_{ray} = 9.4977 \times 10^{-3} \left(\frac{1}{\lambda}\right)^4 c^2 \times \exp\left(-\frac{H_{obs}}{7.996}\right) \quad (10)$$

$$c = 0.23465 + \left(\frac{1.076 \times 10^2}{146 - (1/\lambda^2)}\right) + \left(\frac{0.93161}{41 - (1/\lambda^2)}\right) \quad (11)$$

395 where H_{obs} is the height of the observer, λ is the wavelength in microns, and
 396 "c" is the air's refraction index.

$$A_{aer}(\lambda, h) = A_o \lambda^{-\Sigma} \exp(-H_{obs}/H) \quad (12)$$

397 where H is the density scale height for aerosols and A_o is the total optical
 398 thickness of atmospheric aerosols for $\lambda = 1\mu m$, which depends on the total
 399 content of particles and on their efficiency for scattering and absorption and is
 400 taken to be 0.087 (Walker, 1988; Mohan et al., 1999). Σ is a parameter that
 401 depends on the size of the aerosol particles.

402 Each of these factors (A_{rag}, A_{aer}, A_{oz}) is wavelength dependent and also de-
 403 pends on atmospheric conditions. By convention, by default we have considered
 404 the aerosol content conditions of the AERONET (Holben et al., 1998) Madrid
 405 station on the 29th March 2012 (AOD340 = 0.333, AOD380 = 0.305, AOD440
 406 = 0.251, AOD500 = 0.208, AOD675 = 0.127, AOD870 = 0.084, AOD1020 =
 407 0.066), interpolated for the center of the Nikon bands. We use Rayleigh (1899)
 408 to consider the Rayleigh scattering (equation 10), Stalin et al. (2008) to consider
 409 the aerosols (equation 12) and Hayes and Latham (1975) to consider the Ozone
 410 absorption (A_{oz} factor). To correct for all of these effects equation 8 should be
 411 applied to each pixel of the image. Currently, the aerosol content correction
 412 is only accurate for a narrow field of view, for a wide field of view different
 413 AODs would be needed per pixel. In the future, these data could be obtained
 414 from VIIRS products (Huang et al., 2016). Currently, no other nocturnal lights
 415 products provide multispectral aerosol corrections and the only other nocturnal
 416 light product that provides some correction of this nature is the dimensional
 417 panchromatic aerosol corrections from VIIRS VNP46A2 (Román et al., 2018)
 418 that are still in the beta phase.

419 To determine the original location of the ISS we use a photogrammetric
 420 technique. Considering a circle on geographical coordinates, we will obtain an
 421 ellipse on the raw image coordinates. The axis of the ellipse is either coincident
 422 with the direction of observation or perpendicular to the direction of observa-

423 tion. Matching those two directions with the ISS ground track, we obtain two
424 potential solutions for the true nadir of the ISS. Most of the time the minor axis
425 indicates the direction of the true nadir, although, because of lens aberrations
426 and the curvature of the earth, when the ISS astronauts take images very close
427 to the nadir it can be the major axis that will align with the true view direction
428 (see Fig. 6). Most of the time, a visual inspection of the image allows the iden-
429 tification of the true nadir, by looking at the patterns of the streets and how
430 the buildings block the light of the streets.

431 Once we know the true nadir, as the altitude of the ISS is also known, it
432 is straightforward to determine the tilt angle (we define the tilt angle as that
433 between the nadir and the view angle of the center of the image). Then, the
434 atmospheric extinction can be determined using the approach used in astronomy
435 because of the Helmholtz reciprocity law, the same extinction that an observer
436 has looking to the ISS from a location A is what an observer on the ISS has
437 looking to location A. As the lens used may have a very wide field of view,
438 the distance from the ISS to the ground can be significantly different from one
439 part of an image to another, so we calculate this extinction for each pixel of the
440 image.

441 In some ISS images of the Earth at night, high thin clouds, fog, etc are
442 apparent. These are challenging to address in the generic pipeline described
443 here, and may require more of a case-by-case approach, employing available
444 tools. So, currently, we recommend discarding any areas where the Point Spread
445 Function (PSF) of the emission sources is not homogeneous.

446 *3.2. Step 8: Intercalibration*

447 For a variety of reasons, there may be some systematic differences in the ex-
448 trapolation of the calibration with stars. One of the main unknowns in analysing
449 an image taken from the ISS is which window was used. Sometimes this can be
450 determined because of the date on which the image was obtained or because the
451 image was taken using the Nightpod, which is always used at the main Cupola
452 window. The most popular windows are the Cupola, Window Observational

453 Research Facility (WORF), and Window 7 of the Zvezda module. The Cupola
454 and WORF window have very similar transmission characteristics and so, in
455 principle, should not create differences in colour, although some ESA contacts
456 have reported lower transmission of the WORF. This effect is explained mainly
457 because of the Cupola scratch pane, that is not always in place as it is remov-
458 able. Window 7 of the Zvezda module is comparable although it is even more
459 transparent in principle as it is also UV and IR transparent Pettit (2006); more
460 information about the transmission can be found in ESA (2011) and Stefanov
461 et al. (2017, 2019b). Transmittance can also vary greatly with the angle to the
462 window at which an image was taken. It is typically impossible to know what
463 this angle was, although the geometry of the Cupola, WORF, and Zvezda do
464 not allow acquisitions with very shallow angles.

465 Apart from the different windows used, another reason why there may be
466 systematic differences between the extrapolation of the calibration with stars
467 with different lenses is the use of shutters that are not fully open.

468 For these reasons, and possibly others, we might want to intercalibrate
469 different images or calibrate them against another source, such as data from
470 SNPP/VIIRS-DNB. In a future paper we will focus on these techniques.

471 **4. Spain/Madrid: a worked application**

472 Artificial nighttime lighting has been more extensively studied across Spain
473 than almost any other country (Sánchezde Miguel et al., 2014; Kyba et al.,
474 2014; Estrada-García et al., 2016; Oriol et al., 2017; Ges et al., 2018; Tong
475 et al., 2020). To provide a worked example of the calibration of an astronaut
476 photograph, we use a wide angle image of Madrid and its environs (Fig. 7) taken
477 from the ISS (ISS053-E-249189) on 19/11/2017 at 21:51:38 GMT (note: that
478 the database time is incorrect by 1 h in this exceptional case. This is known
479 because the nadir location that corresponds with the RAW EXIF information
480 is in the Pacific Ocean [lat -49.2, -126.2], which is clearly not possible. The 1
481 h corrected location is just ~ 200 km [lat 38.4,lon -6.4]) from the true nadir

482 [lat 37.49,lon -7.77]) and downloaded on 21/05/2020 from NASA's Gateway to
483 Astronaut Photography of Earth (<https://eol.jsc.nasa.gov/>). Fig. 8 shows the
484 RAW image. This is extracted and separated into four different colour images
485 (Fig. 9). These are not linear at the high values, so linearity correction is applied
486 (Fig. 10). Fig. 11 shows the flat field correction that needs to be applied given
487 that the original image was taken with a 24mm lens. The parameters of equation
488 7 are, according to the image metadata and camera model reference Nikon D3s,
489 $T=1/10$, $C0=1$, $C1=1$ for the Green channel, 1.12 for the Red Channel and 0.95
490 for the Blue Channel, $ISO=5000$, $BN=4$, and $Tn=1.050$.

491 Photometric calibration was carried out for the colour images using the stars
492 (Fig. 12), followed by georeferencing (Fig. 13). Once we have the transforma-
493 tion between geographic location and pixel, we can generate a map of the view
494 angle of the camera with respect to the ground (Fig. 14), which gives the amount
495 of atmosphere that the light goes through before hitting the sensor. After this
496 correction we have a calibrated image that is internally radiometrically coher-
497 ent and colour coherent (Fig. 15). This could now be compared with other ISS
498 images and intercalibrated with them using reference points or compared with
499 VIIRS images. 102 control points were used with an RSME of ~ 4 pixels (due
500 to the large deformation of the image, the pixels closer to the nadir have higher
501 precision, and points close to the horizon less. Also, the ISS sampling is 3 times
502 higher than that of the reference from VIIRS, so it is natural that the image
503 cannot have higher accuracy than the pixel size of the reference layer).

504 Fig 16 and Fig 17 show how this calibrated ISS image compares to a VIIRS
505 image. The comparison is not simple as the sensors used have different spectral
506 sensitivity, different flyby times and were obtained at different angles, and there
507 are not sufficient calibrated ISS images yet fully to determine any systematic
508 differences between the emissions detected in ISS and VIIRS data. fig.18 shows
509 that in comparing the calibrated ISS image of Madrid and VIIRS data the main
510 differences are due to small georeferencing/resolution issues, and light sources
511 that are visible on one image but not the other because of the time of acquisition
512 or the tilt. Nonetheless, despite in the present example there being a 1 month

513 difference in the timing of acquisition of the data, 4 h difference in the flyby
 514 time, spectral sensitivity difference, and difference in spatial resolution, there
 515 is predominantly a linear relationship between the emissions detected by the
 516 two images, and they compare very well. There is an absolute offset between
 517 the two of a factor 1.92. This could be explained by several factors, including
 518 dimming of the streetlights of Madrid after midnight.

519 5. Madrid: ISS-ISS intercalibration

520 In order to examine the performance of the calibration of ISS imagery, we
 521 selected four images of Madrid (see fig. 19). All were acquired before a major
 522 street lighting change took place in the city in 2014 (Robles et al., 2021).

File	Tilt	Exp T.	f/	ISO	Lens	Cam	Time
iss030e292893	7.0	1/50	2.8	10000	180mm f/2.8 D	D3S	2012:02:08 21:09:16.87
iss030e292895	4.0	1/50	2.8	10000	180mm f/2.8 D	D3S	2012:02:08 21:09:02.37
iss031e095634	7.0	1/50	1.4	3200	85mm f/1.4 D	D3S	2012:06:04 22:26:49
iss035e023371	29.0	1/40	3.2	51200	400mm f/2.8	D3S	2013:04:18 22:10:09.73

Table 1: Specifications of the images used for comparison.

523 The two first images were obtained a few seconds from each other, but with
 524 small changes of view angle and exactly the same camera settings, so they are
 525 probably as similar as images taken from the ISS are likely to be. The third
 526 image, was obtained with a different lens, ISO and aperture settings, and was
 527 acquired 1 h and 30 min later, but with a similar view angle. The fourth image
 528 was again obtained with a different lens, ISO, aperture and view angle, still in
 529 the same daily time frame, but more than one year apart. A 5 pixel Gaussian
 530 blur was applied to each image to minimize effects of errors in georeferencing.

531 R2 values for the pixel by pixel comparison of light intensities determined
 532 from the four images varied between 0.88 and 0.98 (Table 2), with the majority of
 533 data points lying close to the 1:1 line (Figure 20). The differences in intensities
 534 between images increase with variation in how those images were acquired.

535 Given the challenges of nocturnal remote sensing that result from the nature
 536 of the light sources (Tong et al., 2020), we conclude that these are satisfactory
 537 results and comparable to findings for panchromatic data from satellite sensors
 538 (Coesfeld et al., 2018).

Ref \ Pro	iss030e292893	iss030e292895	iss031e095634	iss035e023371
iss030e292893	1	0.98	0.95	0.88
iss030e292895	0.98	1	0.96	0.88
iss031e095634	0.95	0.96	1	0.88
iss035e023371	0.88	0.88	0.88	1

Table 2: R^2 values corresponding to the plots fig 20.

539 6. Conclusion

540 Calibration of nighttime images of the Earth taken by astronauts aboard the
 541 ISS is not, in general, an easy task. These images were never designed to provide
 542 remote sensing data. However, if handled properly, they can provide multispec-
 543 tral information on the distribution and change in nighttime lighting that is not
 544 available from any other source, and at spatial resolutions that are compara-
 545 ble or better than those obtained by the DMSP-OLS and SNPP/VIIRS-DNB
 546 platforms. Reflection correction is not needed and we did not apply it because
 547 most studies of light pollution are concerned with the total light received. Also,
 548 in urban areas the vast majority of the surfaces are asphalt and concrete, and
 549 such grey materials do not change significantly the spectral characteristics of
 550 the light.

551 As we have laid out, the correct calibration of nighttime images of the Earth
 552 from the ISS requires processing through a number of steps (Fig. 1). Whilst
 553 some of these undoubtedly have more significant effects on the final image than
 554 others, we recommend that all are carried out, as their influences on different
 555 images can vary greatly.

556 Calibration of nighttime images of the Earth taken from the ISS opens up
557 enormous possibilities for studying the spatial occurrence of artificial lighting
558 and how this is changing with time (nightly, through the year, and across years).
559 Determining how the spatial and temporal variation covaries and determining
560 the influences on other factors (e.g. human health and environmental impacts) is
561 of great interest. As we have previously shown, by using colour-colour diagrams,
562 inferences can also be drawn as to how differences and changes in the lighting
563 technologies being used give rise to these spatio-temporal dynamics (Sánchez de
564 Miguel et al., 2019).

565 **7. Acknowledgements**

566 We thank R. Moore of the Image Science and Analysis Group, NASA John-
567 son Space Center for information on ISS cameras and window properties. We
568 thank Lucía García for her help with improving some figures. We also thank the
569 anonymous reviewers for their constructive feedback. This work was supported
570 by the EMISSI@N project (NERC grant NE/P01156X/1), Fonds de Recherche
571 du Québec : Nature et Technologies (FRQNT), COST (European Cooperation
572 in Science and Technology) Action ES1204 LoNNe (Loss of the Night Network),
573 the ORISON project (H2020-INFRA-SUPP-2015-2), the Cities at Night project,
574 FPU grant from the Ministerio de Ciencia y Tecnología and F. Sánchez de
575 Miguel.

576 Cameras were tested at Laboratorio de Investigación Científica Avanzada
577 (LICA), a facility of UCM-UPM funded by the Spanish program of Interna-
578 tional Campus of Excellence Moncloa (CEI). We acknowledge the support of
579 the Spanish Network for Light Pollution Studies (MINECO AYA2011-15808-E)
580 and also from STARS4ALL, a project funded by the European Union H2020-
581 ICT-2015-688135. This work has been partially funded by the Spanish MICINN,
582 (AyA2018-RTI-096188-B-I00), and by the Madrid Regional Government through
583 the TEC2SPACE-CM Project (P2018/NMT-4291).

584 The ISS images are courtesy of the Earth Science and Remote Sensing Unit,

585 NASA Johnson Space Center. Thanks to S. Doran for helping us to locate the
586 missing image that we use as an example. We are very grateful to all members
587 of the crews of the ISS from all agencies, NASA, ESA, JAXA, CSA-ASC and
588 ROSCOSMOS, for their images.

589 **Description of author's responsibilities**

590 A.S.M., J.Z., J.G., M.A., D.R.P., J.B. and K.J.G. conceived the study,
591 A.S.M., M.A. and J. Z. conducted the calibration procedures, A.S.M., F.O. and
592 J.Z. analyzed the results, D.R.P. acquired very many of the images used, and
593 designed and developed the basic techniques for the acquisition of images and
594 documented the ISS specifications, W.L.S. led the Earth Science and Remote
595 Sensing Unit, NASA Johnson Space Center and provided key technical infor-
596 mation, and A.S.M., K.J.G. and J.Z. wrote the original manuscript, A.S.M,
597 J.Z., J.G., W.L.S., J.B. and K.J.G. conducted the funding requests. All authors
598 reviewed the manuscript.

599 **Declaration of interest**

600 A.S.M., J.Z. and K.J.G. are members of environmental organizations, in-
601 cluding Bird Life, Celfosc and the International Dark-Sky Association. A.S.M.
602 occasionally provides consultancy advice for the Instituto de Astrofísica de An-
603 dalucia - CSIC and the company SaveStars Consulting S.L.

604 **References**

605 Anderson, S.J., Tuttle, B.T., Powell, R.L., Sutton, P.C., 2010. Characterizing
606 relationships between population density and nighttime imagery for denver,
607 colorado: issues of scale and representation. *International Journal of Remote*
608 *Sensing* 31, 5733–5746.

- 609 Bará, S., Rodríguez-Arós, Á., Pérez, M., Tosar, B., Lima, R.C., Sánchez de
610 Miguel, A., Zamorano, J., 2019. Estimating the relative contribution of street-
611 lights, vehicles, and residential lighting to the urban night sky brightness.
612 *Lighting Research & Technology* 51, 1092–1107.
- 613 Bará, S., 2020. Niveis de iluminación de referencia para as diferentes zonas
614 da rede natura 2000 de galicia, tecnoloxías de iluminación e tecnoloxías e
615 procedementos de monitorización e seguimento. URL: [https://doi.org/
616 10.5281/zenodo.3981095](https://doi.org/10.5281/zenodo.3981095), doi:10.5281/zenodo.3981095.
- 617 Borovička, J., Koten, P., Šrbený, L., Štork, R., Hornoch, K., 2014. Spectral,
618 photometric, and dynamic analysis of eight draconid meteors. *Earth, Moon,
619 and Planets* 113, 15–31.
- 620 Burggraaff, O., Schmidt, N., Zamorano, J., Pauly, K., Pascual, S., Tapia, C.,
621 Spyrakos, E., Snik, F., 2019. Standardized spectral and radiometric calibra-
622 tion of consumer cameras. *Optics express* 27, 19075–19101.
- 623 Cardiel, N., Gorgas, J., Gallego, J., Serrano, A., Zamorano, J., Garcia-Vargas,
624 M.L., Gomez-Cambronero, P., Filgueira, J.M., 2002. Proper handling of ran-
625 dom errors and distortions in astronomical data analysis, in: *Astronomical
626 Data Analysis II*, International Society for Optics and Photonics. pp. 297–304.
- 627 Cardiel, N., Zamorano, J., Bará, S., Sánchez de Miguel, A., Cabello, C., Gallego,
628 J., García, L., González, R., Izquierdo, J., Pascual, S., et al., 2021. Synthetic
629 rgb photometry of bright stars: definition of the standard photometric system
630 and ucm library of spectrophotometric spectra. *Monthly Notices of the Royal
631 Astronomical Society* 504, 3730–3748.
- 632 Cheng, S., Cheng, S., 2011. Meteor spectral observation with dslr, normal lens
633 and prism. *WGN, Journal of the International Meteor Organization* .
- 634 Chylinski, R., 2012. *Time-lapse Photography: A Complete Introduction to
635 Shooting, Processing, and Rendering Time-lapse Movies with a DSLR Cam-
636 era*. LearnTimelapse. com.

637 Cities at night collaboration, 2015. Dark skies catalog: Mix. URL: [https://pmisson.carto.com/viz/fe1a723a-fa81-11e4-bb11-0e018d66dc29/
638 public_map](https://pmisson.carto.com/viz/fe1a723a-fa81-11e4-bb11-0e018d66dc29/public_map).
639

640 Coesfeld, J., Anderson, S.J., Baugh, K., Elvidge, C.D., Schernthanner, H.,
641 Kyba, C., 2018. Variation of individual location radiance in viirs dnb monthly
642 composite images. *Remote Sensing* 10, 1964.

643 Coffin, D., 2008. Ddraw: Decoding raw digital photos in linux. URL:
644 <http://cybercom.net/~dcoffin/dcraw> 81.

645 Crameri, F., 2021. Scientific colour maps. URL: [https://doi.org/10.5281/
646 zenodo.4491293](https://doi.org/10.5281/zenodo.4491293), doi:10.5281/zenodo.4491293.

647 Desk, A.D., 1992. Tiff. URL: [https://ftp.nice.ch/pub/next/developer/
648 resources/libraries/_tiff.3.0b.s/tiff/doc/_TIFF6.pdf](https://ftp.nice.ch/pub/next/developer/resources/libraries/_tiff.3.0b.s/tiff/doc/_TIFF6.pdf).

649 Ducati, J., 2002. Vizier online data catalog: Catalogue of stellar photometry
650 in johnson's 11-color system. yCat URL: [http://vizier.u-strasbg.fr/
651 viz-bin/VizieR?-source=II/237](http://vizier.u-strasbg.fr/viz-bin/VizieR?-source=II/237).

652 Elvidge, C.D., Baugh, K.E., Kihn, E.A., Kroehl, H.W., Davis, E.R., 1997. Map-
653 ping city lights with nighttime data from the dmsp operational linescan sys-
654 tem. *Photogrammetric Engineering and Remote Sensing* 63, 727–734.

655 Elvidge, C.D., Baugh, K.E., Zhizhin, M., Hsu, F.C., 2013. Why viirs data are
656 superior to dmsp for mapping nighttime lights. *Proceedings of the Asia-Pacific
657 Advanced Network* 35, 62.

658 ESA, 2011. Research Announcement for ISS Experiments Relevant To
659 Study Global Climate Change Annex 1: Additional Technical Infor-
660 mation on ISS Capabilities And Background Information. Technical
661 Report. ESA. URL: [http://wsn.spaceflight.esa.int/docs/201107/
662 Annex1-ESA-ISS-CC-A0-Climate-Change.pdf](http://wsn.spaceflight.esa.int/docs/201107/Annex1-ESA-ISS-CC-A0-Climate-Change.pdf).

- 663 Estrada-García, R., García-Gil, Manuel aFnd Acosta, L., Bará, S., Sanchez-de
664 Miguel, A., Zamorano, J., 2016. Statistical modelling and satellite monitoring
665 of upward light from public lighting. *Lighting Research & Technology* 48,
666 810–822.
- 667 Falchi, F., Cinzano, P., Elvidge, C.D., Keith, D.M., Haim, A., 2011. Limiting the
668 impact of light pollution on human health, environment and stellar visibility.
669 *Journal of environmental management* 92, 2714–2722.
- 670 Finckenor, M.M., de Groh, K., 2017. A researcher’s guide to: Space environ-
671 mental effects. *National Aeronautics and Space Administration International*
672 *Space Station Researcher’s Guide Series*, NP-2015-03-015-JSC , 15.
- 673 Fossum, E.R., Mendis, S.K., Pain, B., Nixon, R.H., Zhou, Z., 2000. Active pixel
674 sensor having intra-pixel charge transfer with analog-to-digital converter. US
675 Patent 6,021,172.
- 676 Fowler, B., El Gamal, A., 1995. Cmos image sensor with pixel level a/d conver-
677 sion. US Patent 5,461,425.
- 678 Fulbright, J.P., Xiong, X., 2015. Suomi-npp viirs day/night band calibration
679 with stars, in: *Earth Observing Systems XX*, International Society for Optics
680 and Photonics. p. 96071S.
- 681 García Gil, M., Francia Payàs, P., San Martí Páramo, R., Solano Lamphar, H.,
682 2012. Contaminación lumínica: una visión desde el foco contaminante: el
683 alumbrado artificial. *Universitat Politècnica de Catalunya. Iniciativa Digital*
684 *Politécnica*.
- 685 Garcia-Saenz, A., Sánchez-de Miguel, A., Espinosa, A., Valentin, A., Aragonés,
686 N., Llorca, J., Amiano, P., Martín Sánchez, V., Guevara, M., Capelo,
687 R., Tardón, A., Peiró-Perez, R.o., iménez Moleón, J.J., Roca-Barceló, A.,
688 Pérez-Gómez, B., Dierssen-Sotos, T., Fernández-Villa, T., Moreno-Iribas, C.,
689 Moreno, V., García-Pérez, J., Castaño Vinyals, G., Pollán, M., Aubé, M.,

690 Kogevinas, M., 2018. Evaluating the association between artificial light-at-
691 night exposure and breast and prostate cancer risk in Spain (MCC-Spain study).
692 *Environmental Health Perspectives* 126, 047011.

693 Garcia-Saenz, A., Sánchez de Miguel, A., Espinosa, A., Valentin, A., Aragonés,
694 N., Llorca, J., Amiano, P., Martín Sánchez, V., Guevara, M., Capelo,
695 R., Tardón, A., Peiró-Perez, A., Jiménez-Moleón, J., Roca-Barceló, A.,
696 Pérez-Gómez, B., Dierssen-Sotos, T., Fernández-Villa, T., Moreno-Iribas, C.,
697 Moreno, V., García-Pérez, J., Castaño-Vinyals, G., Pollán, M., Aubé, M.,
698 Kogevinas, M., 2019. Artificial light at night (ALAN), blue light spectrum ex-
699 posure and colorectal cancer risk in Spain (MCC-Spain study). *Environmental*
700 *Epidemiology* 3, 212.

701 Gaston, K.J., 2013. A green light for efficiency. *Nature* 497, 560–561.

702 Gaston, K.J., 2018. Lighting up the nighttime. *Science* 362, 744–746.

703 Gaston, K.J., Davies, T.W., Bennie, J., Hopkins, J., 2012. Reducing the eco-
704 logical consequences of night-time light pollution: options and developments.
705 *Journal of Applied Ecology* 49, 1256–1266.

706 Gaston, K.J., Gaston, S., Bennie, J., Hopkins, J., 2015. Benefits and costs of
707 artificial nighttime lighting of the environment. *Environmental Reviews* 23,
708 14–23.

709 Geographics, B.M., 2011. Global Mapper. URL: <http://www.blumarblegeo.com/products/global-mapper.php>.

711 Ges, X., Bará, S., García-Gil, M., Zamorano, J., Ribas, S.J., Masana, E., 2018.
712 Light pollution offshore: Zenithal sky glow measurements in the Mediter-
713 ranean coastal waters. *Journal of Quantitative Spectroscopy and Radiative*
714 *Transfer* 210, 91–100.

715 Hale, J.D., Arlettaz, R., 2019. Artificial lighting and biodiversity in Switzer-
716 land. URL: [http://www.darksky.ch/dss/wp-content/uploads/2019/02/](http://www.darksky.ch/dss/wp-content/uploads/2019/02/Artificial-lighting-End-Report-V4.pdf)
717 [Artificial-lighting-End-Report-V4.pdf](http://www.darksky.ch/dss/wp-content/uploads/2019/02/Artificial-lighting-End-Report-V4.pdf).

718 Hänel, A., Posch, T., Ribas, S.J., Aubé, M., Duriscoe, D., Jechow, A., Kollath,
719 Z., Lolkema, D.E., Moore, C., Schmidt, N., et al., 2018. Measuring night sky
720 brightness: methods and challenges. *Journal of Quantitative Spectroscopy*
721 *and Radiative Transfer* 205, 278–290.

722 Hanisch, R.J., Farris, A., Greisen, E.W., Pence, W.D., Schlesinger, B.M.,
723 Teuben, P.J., Thompson, R.W., Warnock, A., 2001. Definition of the flexible
724 image transport system (fits). *Astronomy & Astrophysics* 376, 359–380.

725 Harwit, M., 1973. *Astrophysical concepts*. Wiley, New York.

726 Hayes, D.S., Latham, D., 1975. A rediscussion of the atmospheric extinction and
727 the absolute spectral-energy distribution of vega. *The Astrophysical Journal*
728 197, 593–601.

729 Hog, E., Fabricius, C., Makarov, V.V., Urban, S., Corbin, T., Wycoff, G.,
730 Bastian, U., Schwekendiek, P., Wicenec, A., 2000. The Tycho-2 catalogue of
731 the 2.5 million brightest stars. Technical Report. NAVAL OBSERVATORY
732 WASHINGTON DC.

733 Holben, B.N., Eck, T.F., Slutsker, I.a., Tanre, D., Buis, J., Setzer, A., Ver-
734 mote, E., Reagan, J.A., Kaufman, Y., Nakajima, T., et al., 1998. Aeronet—a
735 federated instrument network and data archive for aerosol characterization.
736 *Remote sensing of environment* 66, 1–16.

737 Hölker, F., Moss, T., Griefahn, B., Kloas, W., Voigt, C.C., Henckel, D., Hänel,
738 A., Kappeler, P.M., Völker, S., Schwope, A., et al., 2010. The dark side of
739 light: a transdisciplinary research agenda for light pollution policy. *Ecology*
740 *and Society* 15.

741 Huang, J., Kondragunta, S., Laszlo, I., Liu, H., Remer, L.A., Zhang, H., Su-
742 perczynski, S., Ciren, P., Holben, B.N., Petrenko, M., 2016. Validation and
743 expected error estimation of suomi-npp viirs aerosol optical thickness and
744 ångström exponent with aeronet. *Journal of Geophysical Research: Atmo-*
745 *spheres* 121, 7139–7160.

- 746 ISO 12232:2006 (E), 2006. Photography — Digital still cameras — Determina-
747 tion of exposure index, ISO speed ratings, standard output sensitivity, and
748 recommended exposure index. Standard. International Organization for Stan-
749 dardization. Geneva, CH.
- 750 Kotarba, A.Z., Aleksandrowicz, S., 2016. Impervious surface detection with
751 nighttime photography from the international space station. *Remote Sensing*
752 of Environment 176, 295–307.
- 753 Koyama, H., Jiang, H., 2011. Development of digital slr camera nikon d3s.
754 *JSPST* 73, 94–98.
- 755 Kuechly, H.U., Kyba, C.C., Ruhtz, T., Lindemann, C., Wolter, C., Fischer,
756 J., Hölker, F., 2012. Aerial survey and spatial analysis of sources of light
757 pollution in berlin, germany. *Remote Sensing of Environment* 126, 39–50.
- 758 Kyba, C., Garz, S., Kuechly, H., Sánchez de Miguel, A., Zamorano, J., Fischer,
759 J., Hölker, F., 2014. High-resolution imagery of earth at night: new sources,
760 opportunities and challenges. *Remote Sensing* 7, 1–23.
- 761 Kyba, C.C., Kuester, T., De Miguel, A.S., Baugh, K., Jechow, A., Hölker, F.,
762 Bennie, J., Elvidge, C.D., Gaston, K.J., Guanter, L., 2017. Artificially lit
763 surface of earth at night increasing in radiance and extent. *Science advances*
764 3, e1701528.
- 765 Lang, D., Hogg, D.W., Mierle, K., Blanton, M., Roweis, S., 2010. Astrometry.
766 net: Blind astrometric calibration of arbitrary astronomical images. *The*
767 *astronomical journal* 139, 1782.
- 768 Levin, N., Duke, Y., 2012. High spatial resolution night-time light images for
769 demographic and socio-economic studies. *Remote Sensing of Environment*
770 119, 1–10.
- 771 Levin, N., Kyba, C.C., Zhang, Q., de Miguel, A.S., Román, M.O., Li, X.,
772 Portnov, B.A., Molthan, A.L., Jechow, A., Miller, S.D., et al., 2020. *Remote*

773 sensing of night lights: A review and an outlook for the future. *Remote*
774 *Sensing of Environment* 237, 111443.

775 Li, X., Ge, L., Chen, X., 2014. Quantifying contribution of land use types
776 to nighttime light using an unmixing model. *IEEE Geoscience and Remote*
777 *Sensing Letters* 11, 1667–1671.

778 Liu, Q., Sutton, P.C., Elvidge, C.D., 2011. Relationships between nighttime
779 imagery and population density for hong kong. *Proc. Asia-Pac. Adv. Netw*
780 *31*, 79.

781 Lockwood, J.P., Hazlett, R.W., 2013. *Volcanoes: global perspectives*. John
782 *Wiley & Sons*.

783 Madiedo, J.M., Ortiz, J.L., Morales, N., Santos-Sanz, P., 2019. Multiwavelength
784 observations of a bright impact flash during the 2019 january total lunar
785 eclipse. *Monthly Notices of the Royal Astronomical Society* 486, 3380–3387.

786 Mazor, T., Levin, N., Possingham, H.P., Levy, Y., Rocchini, D., Richardson,
787 A.J., Kark, S., 2013. Can satellite-based night lights be used for conservation?
788 the case of nesting sea turtles in the mediterranean. *Biological Conservation*
789 *159*, 63–72.

790 Meier, J.M., 2018. Temporal profiles of urban lighting: Proposal for a research
791 design and first results from three sites in berlin. 10.14279/depositonce-8285
792 .

793 Metcalf, J.P., 2012. Detecting and characterizing nighttime lighting using multi-
794 spectral and hyperspectral imaging. Ph.D. thesis. Monterey, California. Naval
795 Postgraduate School. URL: [https://apps.dtic.mil/dtic/tr/fulltext/
796 u2/a578620.pdf](https://apps.dtic.mil/dtic/tr/fulltext/u2/a578620.pdf).

797 Sánchez de Miguel, A., Castaño, J.G., Zamorano, J., Pascual, S., Ángeles, M.,
798 Cayuela, L., Martinez, G.M., Challupner, P., Kyba, C.C., 2014. Atlas of
799 astronaut photos of earth at night. *Astronomy & Geophysics* 55, 4–36.

- 800 Mohan, V., Uddin, W., Sagar, R., Gupta, S., 1999. Atmospheric extinction at
801 devasthal, naini tal. Bulletin of the Astronomical Society of India , 601.
- 802 Nakamura, J.i., Kemeny, S., Fossum, E., 1995. Cmos active pixel image sensor
803 with simple floating gate pixels. IEEE Transactions on Electron Devices 42,
804 1693–1694.
- 805 Ocaña, F., 2017. Techniques for near-earth interplanetary matter detection and
806 characterisation from optical ground-based observatories. (Doctoral disser-
807 tation, Universidad Complutense de Madrid) URL: [https://eprints.ucm.
808 es/47590/](https://eprints.ucm.es/47590/).
- 809 Ocaña, F., de Miguel, A.S., Project, D., et al., 2019. Balloon-borne video
810 observations of geminids 2016. arXiv preprint arXiv:1911.10064 .
- 811 Oliphant, T.E., 2006. A guide to NumPy. volume 1. Trelgol Publishing USA.
- 812 Oriol, N., Colom, L.and Redondo, J., Oriol, J., Rius, J., 2017. La luz de la
813 ciudad. Grup d’Estudis sobre Energia, Territori i Societat, Departament de
814 Geografia, Universitat Autònoma de Barcelona.
- 815 Pauwels, J., Le Viol, I., Azam, C., Valet, N., Julien, J.F., Bas, Y., Lemarchand,
816 C., de Miguel, A.S., Kerbiriou, C., 2019. Accounting for artificial light impact
817 on bat activity for a biodiversity-friendly urban planning. Landscape and
818 Urban planning 183, 12–25.
- 819 Pedregosa, F., Varoquaux, G., Gramfort, A., Michel, V., Thirion, B., Grisel, O.,
820 Blondel, M., Prettenhofer, P., Weiss, R., Dubourg, V., Vanderplas, J., Passos,
821 A., Cournapeau, D., Brucher, M., Perrot, M., Duchesnay, E., 2011. Scikit-
822 learn: Machine learning in Python. Journal of Machine Learning Research
823 12, 2825–2830.
- 824 Pettit, D., 2006. Use of the international space station for observations beneficial
825 to international polar year 2007-2008.

- 826 Pettit, D., 2009. Exploring the frontier: science of opportunity on the interna-
827 tional space station. *Proceedings of the American Philosophical Society* 153,
828 381–402.
- 829 Pickering, K.A., 2002. The southern limits of the ancient star catalog and the
830 commentary of hipparchos. *DIO* 12, 3–27.
- 831 Poddaný, S., Brát, L., Pejcha, O., 2010. Exoplanet transit database. reduction
832 and processing of the photometric data of exoplanet transits. *New Astronomy*
833 15, 297–301.
- 834 Rayleigh, L., 1899. Xxxiv. on the transmission of light through an atmosphere
835 containing small particles in suspension, and on the origin of the blue of the
836 sky. *The London, Edinburgh, and Dublin Philosophical Magazine and Journal*
837 of Science 47, 375–384.
- 838 Rich, C., Longcore, T., 2013. *Ecological consequences of artificial night lighting*.
839 Island Press.
- 840 Robitaille, T.P., Tollerud, E.J., Greenfield, P., Droettboom, M., Bray, E., Ald-
841 croft, T., Davis, M., Ginsburg, A., Price-Whelan, A.M., Kerzendorf, W.E.,
842 et al., 2013. Astropy: A community python package for astronomy. *Astron-*
843 *omy & Astrophysics* 558, A33.
- 844 Robles, J., Zamorano, J., Pascual, S., Sánchez de Miguel, A., Gallego, J., Gas-
845 ton, K.J., 2021. Evolution of brightness and color of the night sky in madrid.
846 *Remote Sensing* 13, 1511.
- 847 Román, M.O., Wang, Z., Sun, Q., Kalb, V., Miller, S.D., Molthan, A., Schultz,
848 L., Bell, J., Stokes, E.C., Pandey, B., et al., 2018. Nasa’s black marble
849 nighttime lights product suite. *Remote Sensing of Environment* 210, 113–
850 143.
- 851 Rybnikova, N., Portnov, B.A., 2018. Population-level study links short-
852 wavelength nighttime illumination with breast cancer incidence in a major
853 metropolitan area. *Chronobiology international* 35, 1198–1208.

854 Rybnikova, N.A., Portnov, B.A., 2017. Remote identification of research and
855 educational activities using spectral properties of nighttime light. *ISPRS*
856 *Journal of Photogrammetry and Remote Sensing* 128, 212–222.

857 Sabbatini, M., 2014. Nightpod-nodding mechanism for the iss. Technical Report.
858 Technical Report Experiment Record.

859 Sakai, S., Tashiro, Y., Akahane, N., Kuroda, R., Mizobuchi, K., Sugawa, S.,
860 2009. A pixel-shared cmos image sensor using lateral overflow gate, in: 2009
861 Proceedings of ESSCIRC, IEEE. pp. 240–243.

862 Sánchez de Miguel, A., 2015. Variacion espacial, temporal y espectral de la
863 contaminacion luminica y sus fuentes: Metodologia y resultados. Ph.D. thesis.
864 Universidad Complutense de Madrid. doi:10.5281/zenodo.1289932.

865 Sánchez de Miguel, A., Aubé, M., Zamorano, J., Kocifaj, M., Roby, J., Tapia, C.,
866 2017. Sky quality meter measurements in a colour-changing world. *Monthly*
867 *Notices of the Royal Astronomical Society* 467, 2966–2979.

868 Sánchez de Miguel, A., Gomez Castano, J., Zamorano, J., Pascual, S., Angeles,
869 M., Cayuela, L., Martin Martinez, G., Challupner, P., Kyba, C., 2014. Atlas
870 of astronaut photos of earth at night. *Astronomy & Geophysics* 55, 36–36.

871 Sánchez de Miguel, A., Kyba, C.C., Aubé, M., Zamorano, J., Cardiel, N., Tapia,
872 C., Bennie, J., Gaston, K.J., 2019. Colour remote sensing of the impact of
873 artificial light at night (i): The potential of the international space station
874 and other dslr-based platforms. *Remote sensing of environment* 224, 92–103.

875 Sánchez de Miguel, A., Kyba, C.C., Zamorano, J., Gallego, J., Gaston, K.J.,
876 2020. The nature of the diffuse light near cities detected in nighttime satellite
877 imagery. *Scientific Reports* 10, 1–16.

878 Sánchezde Miguel, A., Zamorano, J., Castaño, J.G., Pascual, S., 2014. Evolution
879 of the energy consumed by street lighting in spain estimated with DMSP-OLS
880 data. *Journal of quantitative spectroscopy and radiative transfer* 139, 109–
881 117.

882 So, C.w., 2014. Observational studies of contributions of artificial and natu-
883 ral light factors to the night sky brightness measured through a monitoring
884 network in hong kong. HKU Theses Online (HKUTO) .

885 Stalin, C., Hegde, M., Sahu, D., Parihar, P., Anupama, G., Bhatt, B., Prabhu,
886 T., 2008. Night sky at the indian astronomical observatory during 2000-2008.
887 Bull. Astr. Soc. India , 111–127.

888 Stefanov, W., Jones, L., Cameron, A., Vanderbloemen, L., Evans, C., 2019a. A
889 researcher’s guide to: International space station earth observations. Johnson
890 Space Center Publication .

891 Stefanov, W., Jones, L., Cameron, A., Vanderbloemen, L., Evans, C., 2019b.
892 A researcher’s guide to: International Space Station Earth Observations
893 (2nd Edition). Technical Report. Johnson Space Center Publication NP-
894 2019-07-003-JSC. URL: [http://wsn.spaceflight.esa.int/docs/201107/
895 Annex1-ESA-ISS-CC-A0-Climate-Change.pdf](http://wsn.spaceflight.esa.int/docs/201107/Annex1-ESA-ISS-CC-A0-Climate-Change.pdf).

896 Stefanov, W.L., Evans, C.A., Runco, S.K., Wilkinson, M.J., Higgins, M.D.,
897 Willis, K., 2017. Astronaut photography: Handheld camera imagery from
898 low earth orbit. hsa , 847.

899 Straizys, V., 1996. The method of synthetic photometry. Baltic Astronomy 5,
900 459–476.

901 Team, Q.D., et al., 2015. Qgis geographic information system. ver. 2.14. 22.
902 open source geospatial foundation project.

903 Tong, K.P., Kyba, C.C., Heygster, G., Kuechly, H.U., Notholt, J., Kollth, Z.,
904 2020. Angular distribution of upwelling artificial light in europe as observed
905 by suomi–npp satellite. Journal of Quantitative Spectroscopy and Radiative
906 Transfer , 107009.

907 Venzke, E., Sennert, S.K., Wunderman, R., 2009. Reports from the smithso-
908 nian’s global volcanism network, june 2009. Bulletin of Volcanology 71, 1211.

- 909 Walker, M.F., 1988. The effect of solar activity on the v and b band sky
910 brightness. *Publications of the Astronomical Society of the Pacific* 100, 496.
- 911 Waltham, N., 2013. Ccd and cmos sensors, in: *Observing photons in space*.
912 Springer, pp. 423–442.
- 913 Warmerdam, F., 2008. The geospatial data abstraction library, in: *Open source
914 approaches in spatial data handling*. Springer, pp. 87–104.
- 915 Wolfe, W.L., 1998. *Introduction to radiometry*. TT29, SPIE, Bellingham. URL:
916 <https://cds.cern.ch/record/1613508>.
- 917 Xu, Y., Knudby, A., Côté-Lussier, C., 2018. Mapping ambient light at night
918 using field observations and high-resolution remote sensing imagery for studies
919 of urban environments. *Building and Environment* 145, 104–114.
- 920 Zamorano, J., de Miguel, A., Pascual, S., Castaño, J., Ramírez, P., Challupner,
921 P., 2011. Iss nocturnal images as a scientific tool against light pollution. LICA
922 report URL: https://eprints.ucm.es/12729/1/iss_processing_8.pdf.

Model	Kodak DCS760	Nikon D1	Nikon D2Xs	Nikon D3	Nikon D3S	Nikon D4	Nikon D5	Sony Alpha a7S II
Agencies	All	All	All	All	All	All	All	JAXA
Model launch	22/03/2001	15/06/1999	01/06/2006	23/08/2007	4/10/2009	06/01/2012	05/01/2016	11/09/2015
In use at ISS	2002-2007	2004-2006	2008-2014	2009-2012	2010-2015	2015-2017	2017-	2018-
Megapixels	6	3	13	13	13	17	21	12
Sensor format	APS-H	APS-C	APS-C	Full Frame	Full Frame	Full Frame	Full Frame	Full Frame
Sensor type	CCD	CCD	CMOS	CMOS	CMOS	CMOS	CMOS	CMOS
ISO Range	80 - 400	200 - 1600	100 - 800	200 - 6400	200 - 12800	100 - 12800	100 - 102400	100 - 102400
Image format	RAW	RAW	RAW	RAW	RAW + TIFF	RAW	RAW	RAW
Fitting	Nikon F	Nikon F	Nikon F	Nikon F	Nikon F	Nikon F	Nikon F	Sony E
Amplification	1.3x	1.5x	1.5x	1x	1x	1x	1x	1x
Live view	No	No	No	Yes	Yes	Yes	Yes	Yes
Video resolution					1280 x 720	1920 x 1080	3840 x 2160	4K
Storage	PCM CIA	CF	CF	CF	CF	CF,XQD	Dual CF,XQD	SD/SDH/C/SDXC

Table 3: Main characteristics of the most popular cameras used for nighttime photography and video at the ISS. Other cameras have been used but rarely or never for this purpose or only for specific experiments (like Nikon D800E and Nikon D850). More info at: <https://col.jsc.nasa.gov/FAQ>. Source: <https://www.dpreview.com/>.

Table 4: Transmission coefficients for the most popular lenses used at the ISS or in light pollution research, relative to that of the 50mm f/1.4 lens. The values correspond to the ratio between the signal of surface brightness of lambertian reference source illuminated at 4 lux with a tungsten lamp, at 1/60 s and ISO 200 with a Nikon D5, for different lenses. This number is equivalent to the transmission stop (T-stop), but on a linear scale. Source: This work.

Lens	Transmission coefficient
Nikon 180mm f/2.8	0.297
Nikon 85mm f/1.4	1.070
Nikon 85mm f/1.8	0.765
Nikon 50mm f/1.8	0.750
Nikon 50mm f/1.4	1
Nikon 10.5mm f/2.8	0.295
Nikon 24mm f/1.4	1.050
Nikon 400mm f/2.8	0.215
Sigma 8mm f/3.5	0.187
Nikon 200mm f/4	0.136
Nikon 28mm f/1.4	1.630
Nikon 28mm f/2.8	0.326
Nikon 28-70mm f/2.8	0.324
Nikon 14-24mm f/2.8	0.307

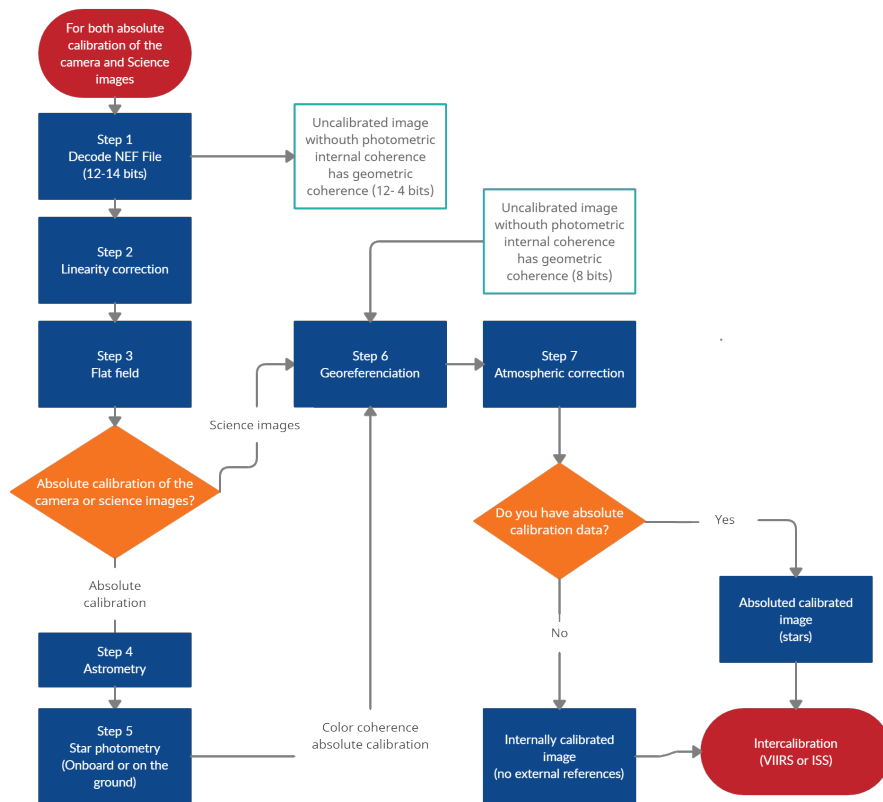


Figure 1: Schema of the potential calibration paths. The red path requires the calibration of the camera using stars. This calibration provides colour coherence and absolute calibration based on stars. The black path indicates what can be done if we do not have an absolute calibrated image with stars, we can alternatively calibrate against the VIIRS-DNB. Some researchers have in the past used the blue path, using just decoded RAW images or even JPG images. We cannot recommend that procedure, as the images will not have internal photometric coherence or colour coherence, they will only have geometric coherence (the degree of incoherence will depend on the lens and dynamic range of the image).

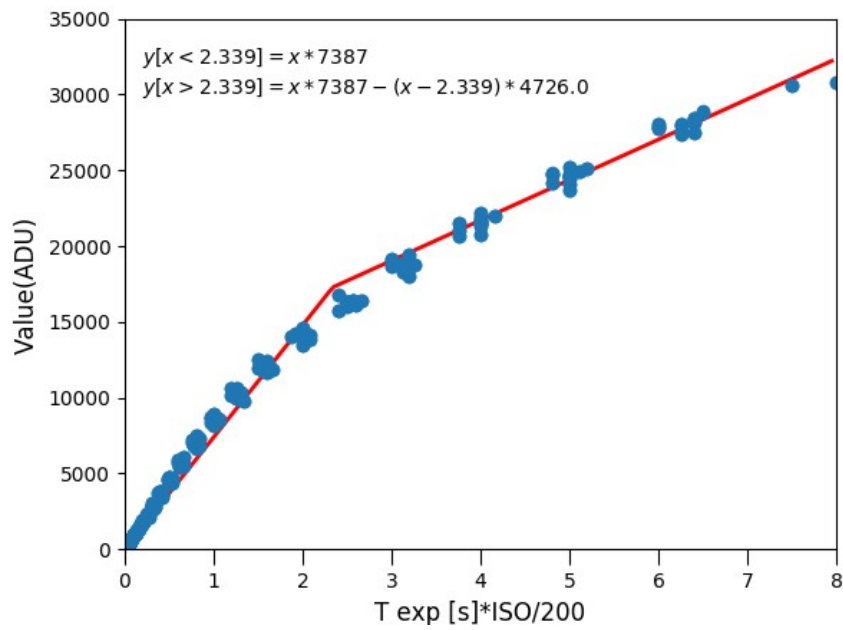


Figure 2: Response of camera to a uniformly lit screen with stabilized source across all ISOs and times of exposure (T) in seconds. The dispersion of the dots is compatible with the errors of the stabilization (0.5%). Response values expressed in dimensionless units (aka ADU). Data calculated with a D5, although compatible with previously calculated data for D3S. Source: this work.

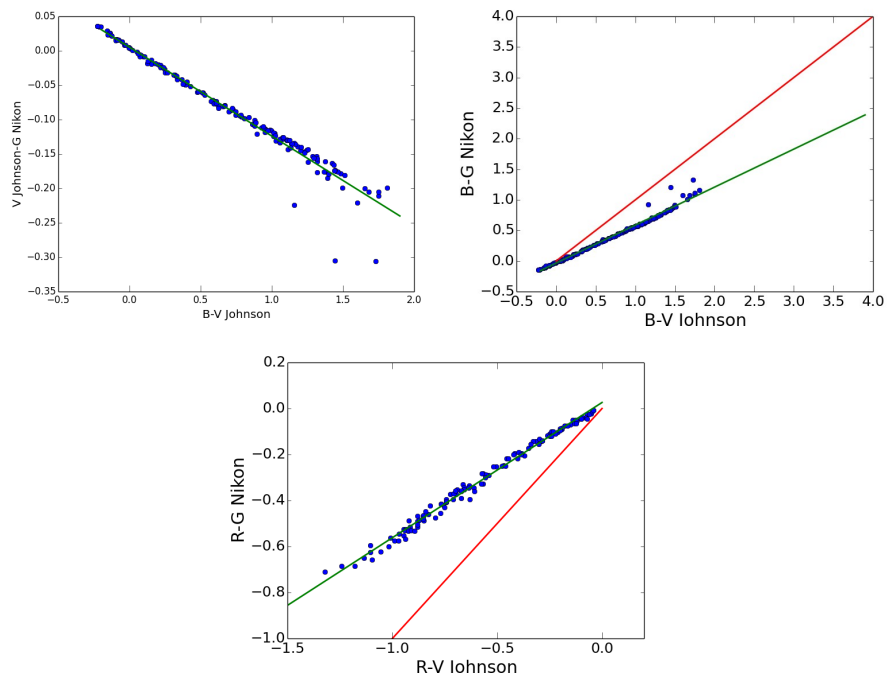


Figure 3: Relationship between emissions in the RVB Johnson bands and the RGB Nikon bands. The 1:1 line is given in red, and the fit to the data in green.

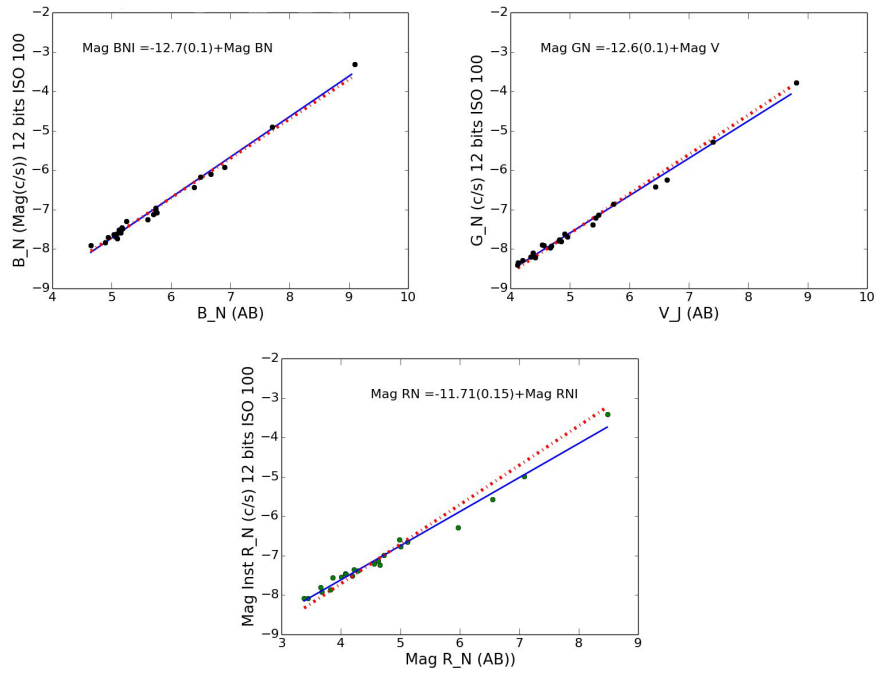


Figure 4: Comparison of the radiance of stars in the Ducati II/237 catalogue with the values determined from calibration images taken with the D3S. Reference (X axis) brightness is in AB magnitudes. Instrumental magnitudes on Y axis. The measurements are in green, the blue line is the fit to all of the data, and the red line the fit excluding outliers using RANSAC.

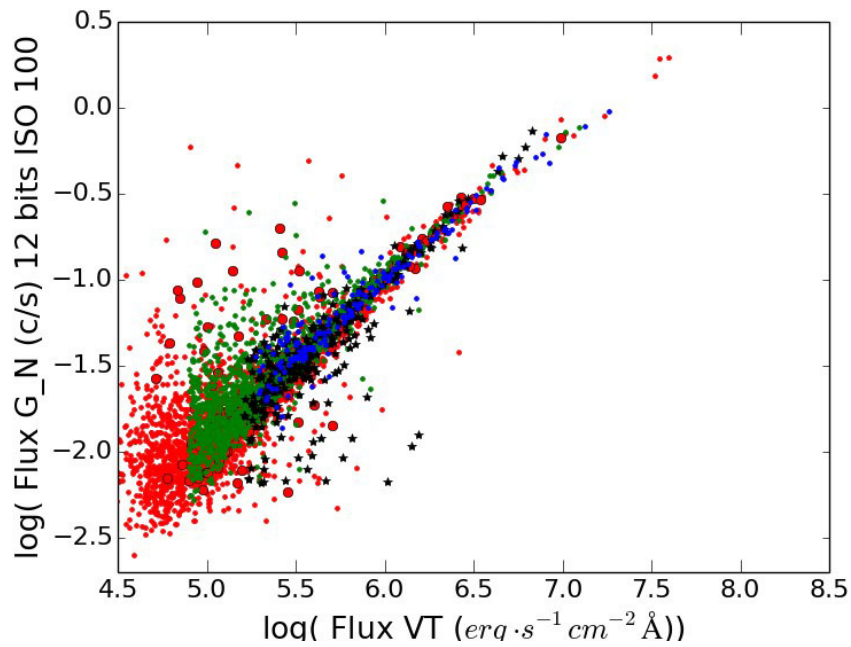


Figure 5: Comparison of the radiance of stars in the Tycho I/259 catalogue with the values determined from calibration images taken with the D3S. Each colour represents a different image, which was obtained using different camera settings (exposure time, ISO). Longer exposure times and higher ISO lead to detection of more stars, but also present more saturation problems for bright stars, as exemplified by the image represented by the small red dots (more details in Sánchez de Miguel (2015)).

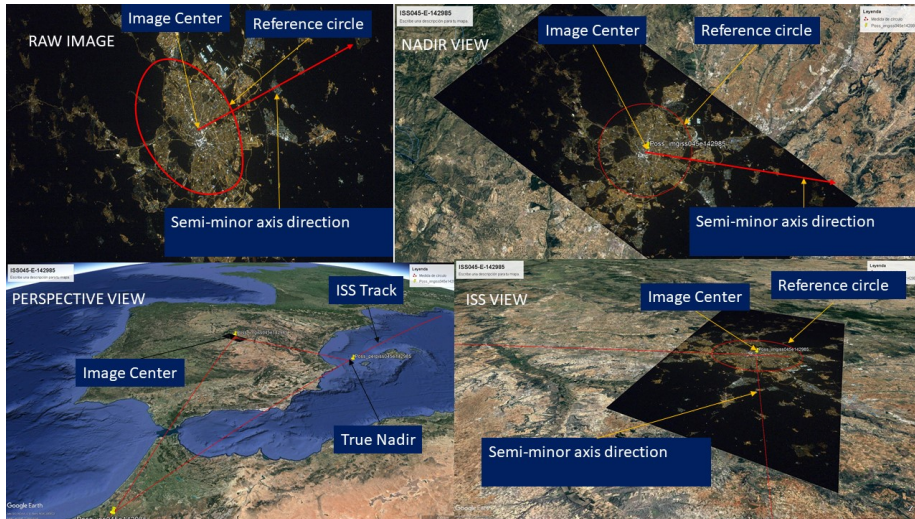


Figure 6: With an ideal nadir view, that is typical of most observations from satellites, an imaginary circle seen from the nadir (top right view), would always be a circle on the ground. But, from a tilted observation, the circle would be transformed, approximately, into an ellipse (top left view and bottom right view), where the minor axis would be in the direction of observation and the major axis will point perpendicular to it. If we intersect view direction with the ground track of the ISS, we can find the true nadir point of observation (bottom left view). We have a first guess of the nadir point of observation thanks to the clock of the camera, but this can have an error as high as 500 km. The deformation is trivial to calculate, for example at the centre of the image, once the image has been georeferenced, using the reverse equations that give us the image coordinates from the ground equations. This simple technique allows us to find the true nadir. In a practical case, once the image is georeferenced, we do not use any target to stabilize the deformation of the image, we can use the georeferentiation formulas to estimate one at the centre of the image of the size that we prefer. In our case, we define a circle of 0.1 km of radius at the centre of the rectified image and we use the deformation formulas to calculate the deformed circle (ellipse).



Figure 7: Original JPG image of Spain used as an exemplar. Madrid (the spider-like lit area) looks to be saturated, although this is not actually the case. This is only one of the reasons not to use JPG images, although geometrically it is equivalent to the RAW image, colours, relative intensities, and other issues like gamma correction mean that this is not recommended.

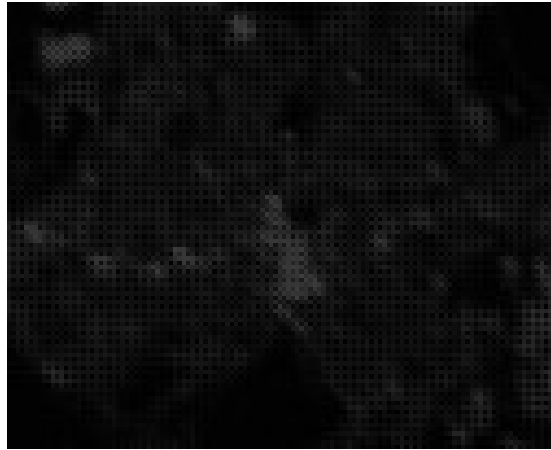


Figure 8: Detail of the center of Madrid on the RAW image of Spain, with the Bayer matrix and the 4 channels merged in one single image. The images do not appear clear because they have not been stretched and the different bands are entangled on the Bayer matrix, as mentioned in the Introduction. It is common for commercial software to use debayering algorithms that can produce artifacts and change the photometry, so we do not use that approach but calibrate each image separately.

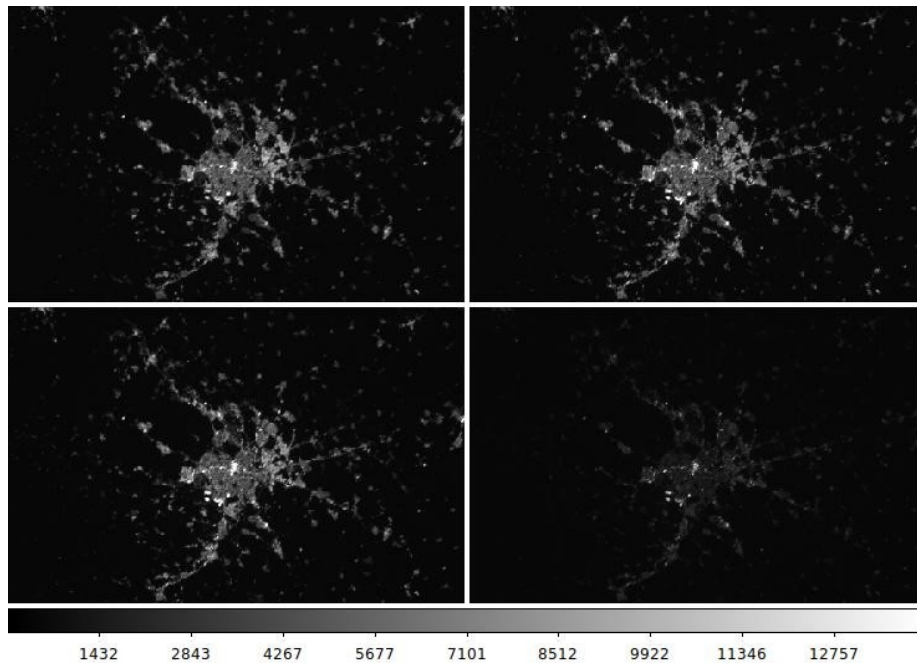


Figure 9: Zoomed detail of Madrid from the exemplar image. The RAW image is extracted and separated into four different images. From top left to bottom right, Red (R1), Green (G2), Green (G3), and Blue (B4) channels.

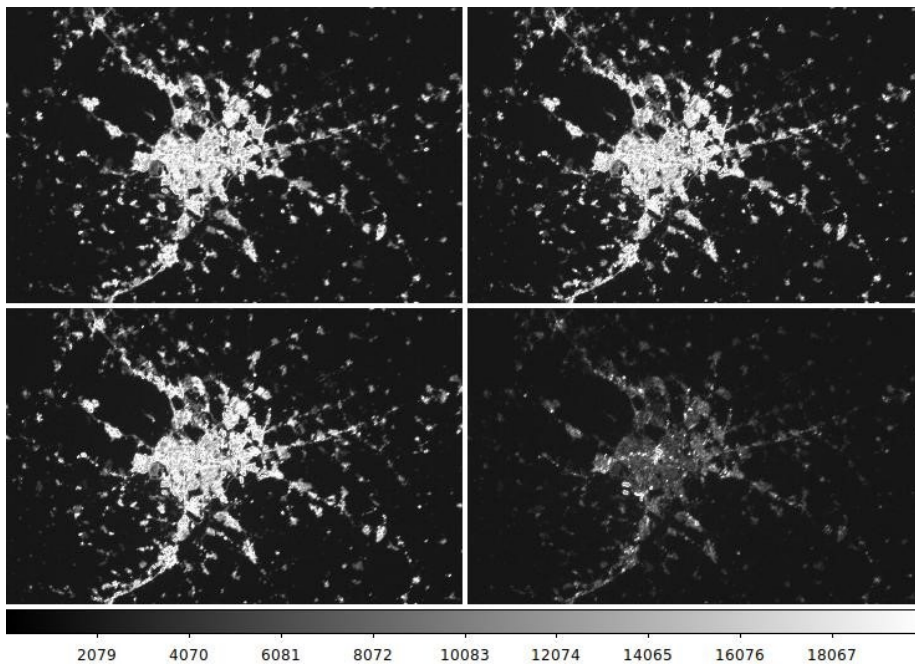


Figure 10: Zoomed detail of the exemplar image, after linearity correction of the four separated channels.

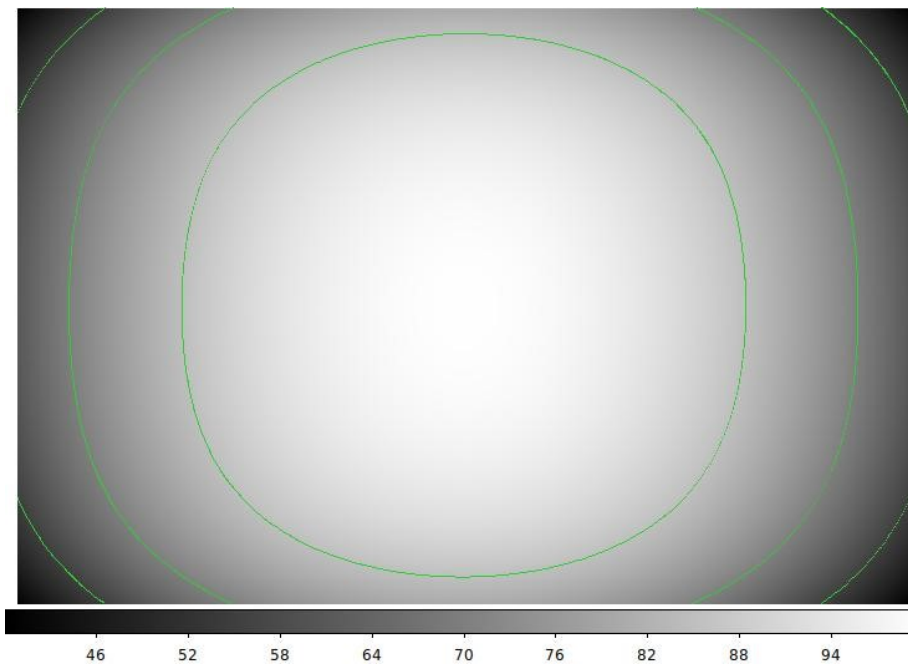


Figure 11: Flat field correction for a 24 mm lens. The intensity at the centre corresponds to 100%, the green lines 85%, 45% and 33%, from inside to outside. Values presented correspond to percentage of the transmission compared with peak.

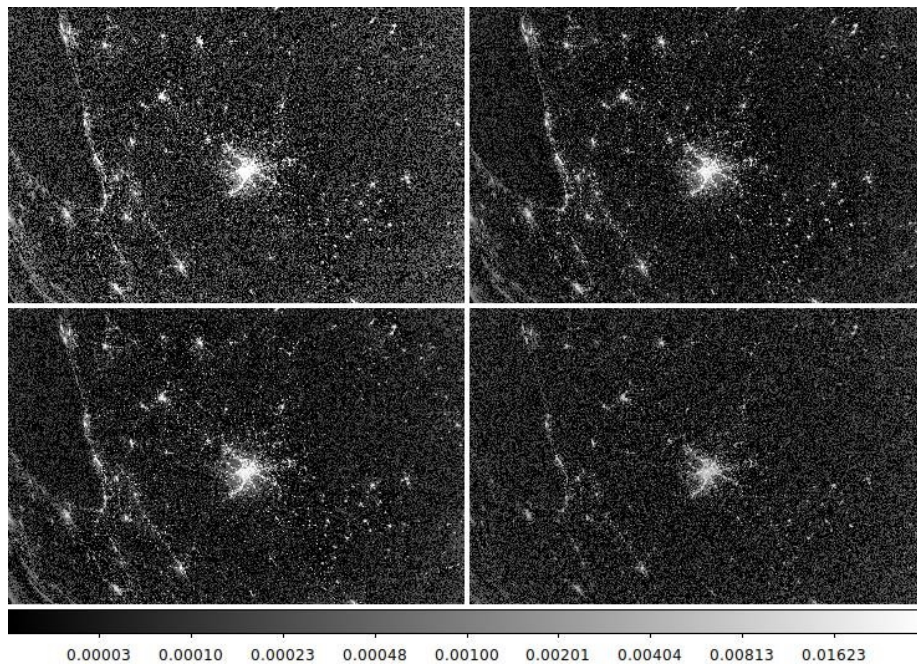


Figure 12: Zoom in (not full picture) from fig 11 after the flat field correction. Results of photometric calibration of the exemplar image. The four extracted channels are now in values of $nW \cdot sr^{-1}cm^{-2}\text{\AA}^{-1}$. This image has not been stretched, so shows a lot of noise from low intensities and cosmic rays.

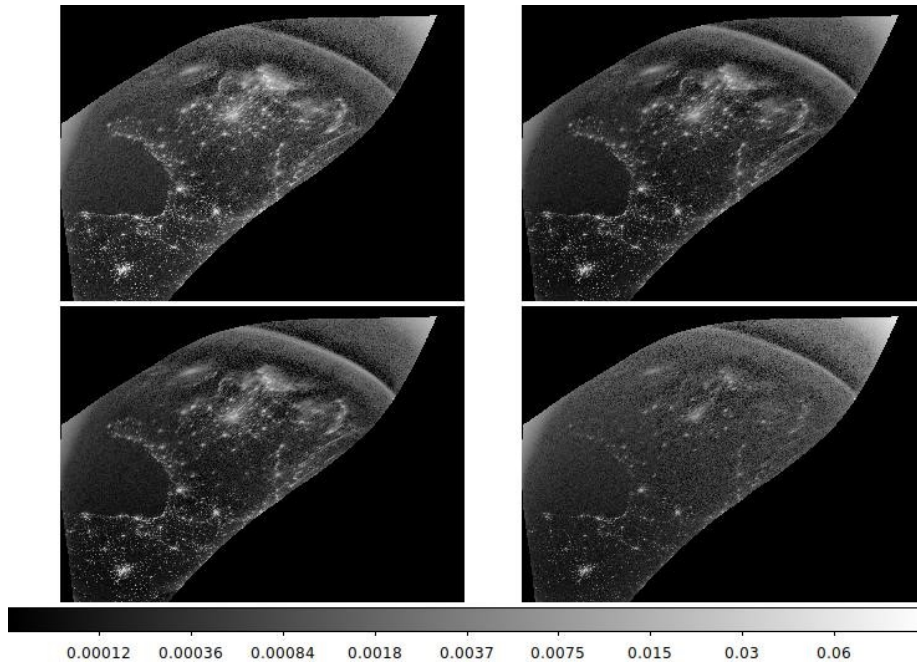


Figure 13: Full picture rectified. The four channel images have to be georeferenced to create correspondence between pixel location and geographical location. This is the same image (Fig. 8), as before, but because the area of the pixels closer to the horizon is larger than for the pixels closer to the nadir, the centre of the image now is France, but this is just a perspective effect. The four extracted channels are now in values of $nW \cdot sr^{-1}cm^{-2}\text{\AA}^{-1}$. This image has not been stretched, so shows a lot of noise from low intensities and cosmic rays.

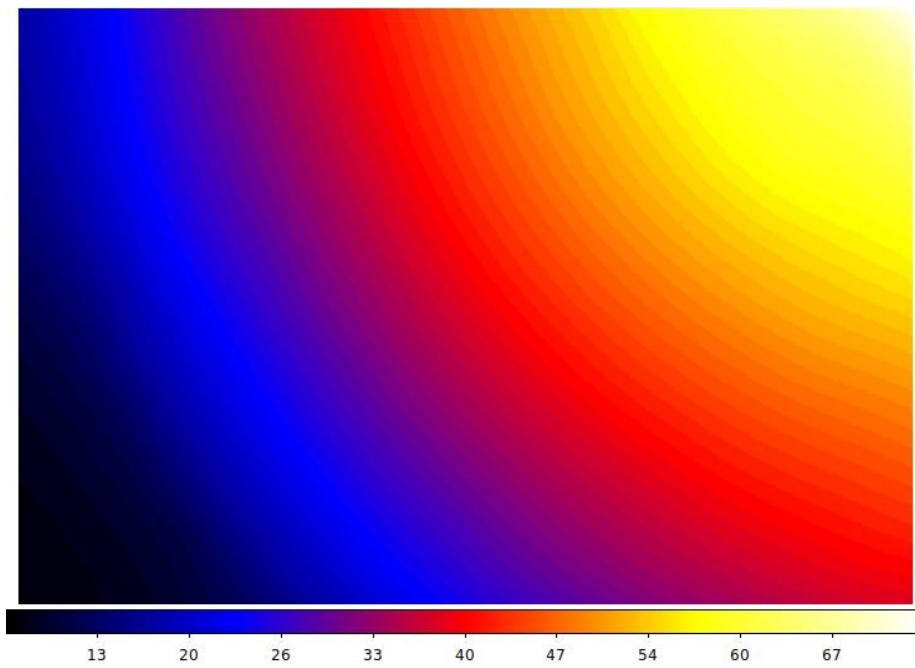


Figure 14: Angular distance to the horizon for the exemplar image. The X and Y axis correspond to the coordinates of the image (see fig 13). These data, along with the altitude and the true nadir, are the basis of the atmospheric correction.



Figure 15: Calibrated version of the exemplar image. Note that artefacts can appear at the edges because the flat field correction enhances noise in those areas. Also, the farther the pixels are from the nadir the blurrier they are. This is because pixels that are closer to the horizon correspond to larger areas than those closer to the nadir, so when the rectification takes place, there is less information in the first ones and errors propagate more than in the second ones. That is why, when several images are available of the same area, it is better to choose those that were acquired with longer focal lengths and closer to the nadir. Units in $nW \cdot sr^{-1}cm^{-2}$. This image has been stretched, so does not show noise as clearly as in the other cases.

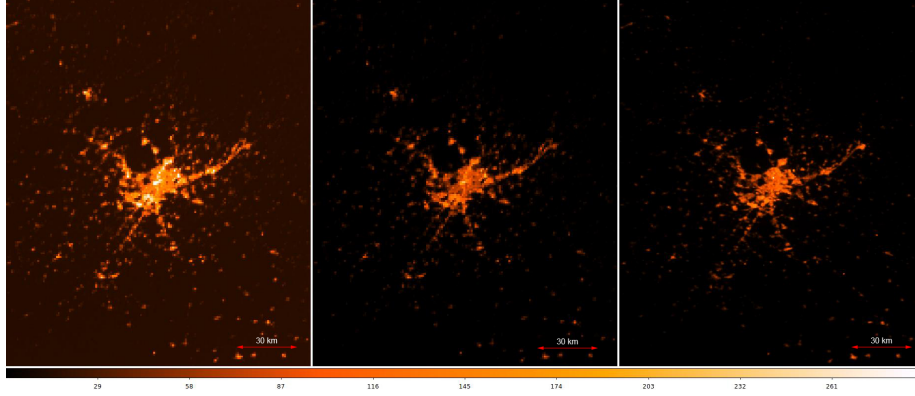


Figure 16: Zoom to Madrid region. Left is the ISS Green band radiance calibrated with stars. Middle image is ISS green band inter-calibrated with VIIRS. Right image is VIIRS comparison image. Units in $nW \cdot sr^{-1}cm^{-2}$. The comparison is between the VIIRS October 2017 (November 2017 has a defect) image EOG average Elvidge et al. (2013) and ISS.

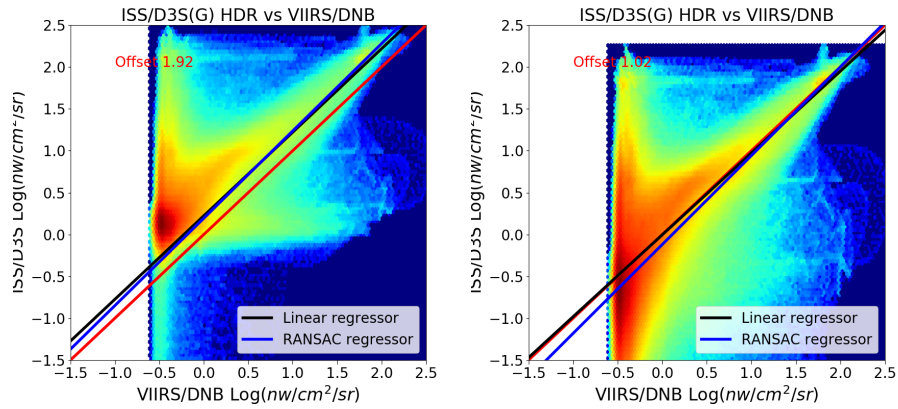


Figure 17: Left: Comparison between VIIRS and ISS Green band star calibrated. Right: Comparison between ISS and VIIRS after background and slope offset. Red line corresponds to 1:1 relationship. Black line, standard linear fit, blue line RANSAC Pedregosa et al. (2011) linear fit. Slope Offset is calculated ratio from $100nW \cdot sr^{-1}cm^{-2}$ ISS compared to corresponding VIIRS equivalent intensity. Background offset corresponds to maximum density points.

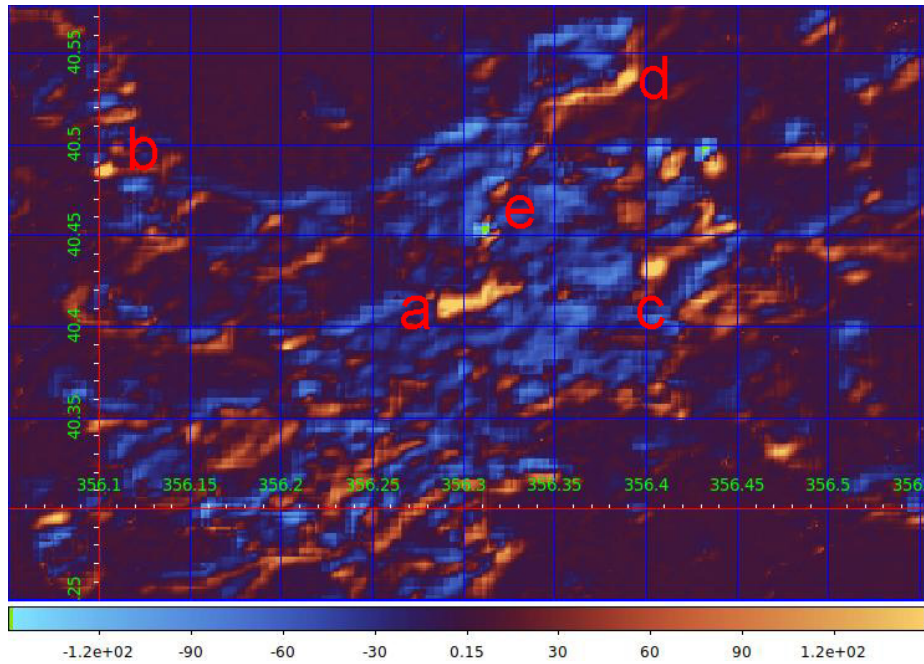


Figure 18: Difference between the VIIRS and ISS image. The main differences are due to time of acquisition of the images. In the ISS image the lights can be seen of the main commercial centers of the Madrid area, the Sol square and surroundings (center of image (a)), the commercial center Gran Plaza 2 (in the west(b)), and the commercial center Plenilunio (in the East (c)) and Plaza Norte (in the north (d)). Also, there is a small difference in the georeferencing. The Santiago Bernabeu Stadium(e) does not appear on the ISS image, probably because of the tilt effect (dark area in the center of the image). Look-up table "Roma" from Crameri (2021).

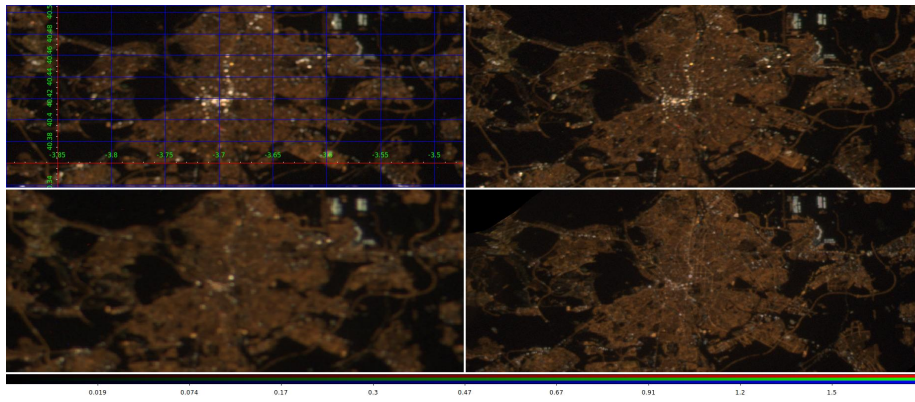


Figure 19: From left to right and top to bottom, the images iss030e292893, iss030e292895, iss031e095634 and iss035e023371. Intensity scale in $nW \cdot sr^{-1} cm^{-2} \text{\AA}^{-1}$. The grid represents latitude and longitude.

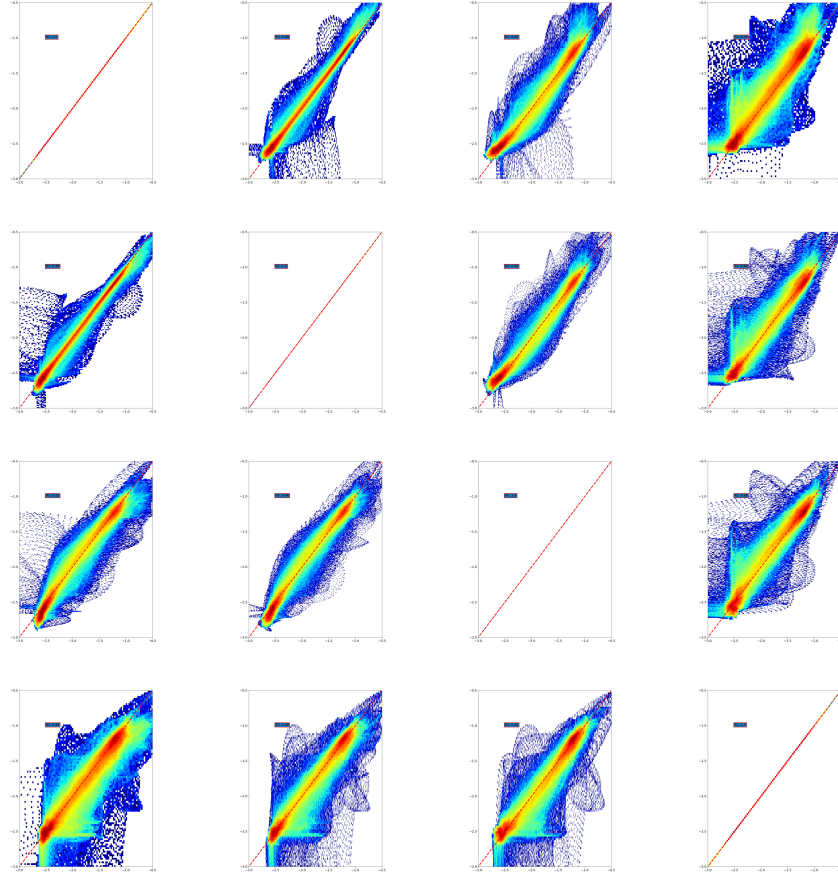


Figure 20: Density plots of the comparison between the images iss030e292893, iss030e292895, iss031e095634 and iss035e023371 on the Green band. The red lines indicate the 1:1 relationship. Units $\log_{10}(nW \cdot sr^{-1} \cdot cm^{-2} \cdot \text{\AA}^{-1})$.